Petrogenesis and tectonic setting of late Paleoproterozoic diorites in the Trans-North China Orogen

Zhiyi Wang [a, b], Jun He [a*], Wolfgang Siebel [b], Shuhao Tang [a], Yiru Ji [a], Jianfeng He [a], Fukun Chen [a]

a: State Key Laboratory of Lithospheric and Environmental Coevolution, School of Earth and Space Sciences, University of Science and Technology of China, Hefei 230026, China

b: Institute of Earth and Environmental Sciences, Albert-Ludwig University Freiburg, Freiburg 79104, Germany

*Corresponding author: jhe1989@ustc.edu.cn (J. He)

Abstract: Unravelling the tectonic setting and evolution of cratons during the late Paleoproterozoic has long been a major focus of geological research. As one of Earth's major cratonic blocks, the North China Craton (NCC) preserves extensive magmatism during this period. Recent investigations have identified numerous 1.78 Ga dioritic intrusions along the southern margin and the center of the NCC. The NCC experienced widespread magmatism at ~1.78 Ga, and the tectonic setting of this period remains unclear and needs better understanding. Diorites of the NCC can help to constrain the late Paleoproterozoic tectonic setting in this region. In this paper we report zircon U-Pb ages of ~1.78 Ga and geochemical data of the Jiguanshan diorite. The diorites in the Trans-North China Orogen and the southern margin of the NCC, including the Jiguanshan diorite, have similar element and isotopic characteristics. The average initial $^{87}Sr/^{86}Sr$ and $\varepsilon_{Nd}(t)$ values are 0.7052 ±0.0003 and -6.5 ±0.2, respectively. The initial Pb isotope compositions of the diorite samples do not show significant enrichment of radiogenic lead. In terms of Sr-Nd-Pb isotope compositions and Nb/Ta, Ba/Th, and Sr/Th ratios, the diorites differ from the coeval Xiong'er volcanic rocks and mafic dike swarms. Our results suggest that the diorites originated from basaltic lower crust, rather than from enriched subcontinental lithospheric mantle. Whole-rock and zircon trace element features indicate that the diorites formed in a rift-related environment. The formation of the diorites reveals a potential transition from late Paleoproterozoic orogenic-related magmatism towards intraplate magmatism.

Key words: Late Paleoproterozoic, North China, Diorite, Zircon, Sr-Nd-Pb isotopes

1 Introduction

North China Ctaton (NCC) was stabilized by the collision and amalgamation of several continental blocks in the late Paleoproterozoic (Fig. 1a; e.g., Zhao and Zhai, 2013; Zhao et al., 2000a, b). Subsequent widespread magmatic activity across the NCC records the cratonization process, providing critical insights into its stabilization and maturation (e.g., Zhai, 2011). The petrogenesis of the Paleoproterozoic magmatic rocks preserves key information about regional tectonic evolution and has been linked to the assembly or breakup of the Columbia supercontinent (e.g., Peng et al., 2007, 2008; Zhao et al., 2009). Among these events, the ~1.78 Ga magmatic event is particularly distinctive due to its large scale, leading to the production of numerous rock types including the Xiong'er Group, A-type granites and mafic dykes (e.g., Cui et al., 2010; Hu et al., 2010; Peng et al., 2007, 2008; Wang et al., 2004; Wang et al., 2014). These rocks are extensively distributed across both the southern margin and Trans-North China Orogen of the NCC. However, the petrogenesis and tectonic setting of these rocks is debated, which revolves around post-collisional/orogenic extension (e.g., Wang et al., 2004, 2008, 2014), continental arc magmatism (e.g., He et al., 2009; Zhao et al., 2009), rifting (e.g., Cui et al., 2010; Zhao et al., 2007), and the involvement of mantle plumes (e.g., Hou et al., 2008; Peng et al., 2007, 2008). Clarifying the tectonic setting during this period is essential for understanding the geological evolution that followed the late Paleoproterozoic amalgamation of the NCC.

In recent years, numerous diorites with ages of *c.* 1780 Ma along the southern margin

of the NCC and Shanxi region (Fig. 1b) have attracted significant attention, potentially offering new perspectives for understanding the tectonic evolution of the craton during the late Paleoproterozoic. These rocks include diorites intruding into Xushan Formation (at *c.* 1789 Ma; Zhao et al., 2004), East-West Group dykes (*c.* 1780 Ma; Peng et al., 2007), Shizhaigou diorite (*c.* 1780 Ma; Cui et al., 2011), Wafang diorite (*c.* 1750 Ma; Wang et al., 2016), Gushicun diorite (*c.* 1780 Ma; Ma et al., 2023a), Muzhijie diorite (*c.* 1780 Ma; Ma et al., 2023b), Fudian diorite (*c.* 1780 Ma; Ma et al., 2023b), and Jiguanshan diorite (*c.* 1780 Ma; this study). The diorites are widely distributed in an approximate east-west trending and possess similar zircon ages. Peng et al. (2007) and Cui et al. (2011) proposed that some of them share identical mantle source regions with the Xiong'er Group volcanic rocks or dyke swarms. Other authors interpret some of them resulting from fractional crystallization (Ma et al., 2023a, b) or from crustal melting with limited mantle influence (Wang et al., 2016). Systematic research of their genesis is crucial for clarifying their formation and constraining the regional geological evolution.

The present study focuses on the Jiguanshan diorite and other diorites with ages between 1.78 and 1.75 Ga from the NCC. These diorites have similar geochemical characteristics, suggesting their formation during a single magmatic episode. By evaluating whole rock geochemical and Sr-Nd-Pb isotopic compositions, as well as Hf isotopic compositions of zircons, a better understanding of the tectonic environment and evolution of the NCC during the late Paleoproterozoic is provided.

2 Geological background and sample description

The NCC records geological evolution since 3.8 Ga ago (e.g., Geng et al., 2012; Liu et al., 1992). It consists of an Archean to Paleoproterozoic metamorphic basement lithologies overlain by Mesoproterozoic unmetamorphosed sedimentary cover (e.g., Lu et al., 2008; Zhao and Zhai, 2013). The crystalline basement is composed of serval microcontinental blocks (Fig. 1a; Zhao et al., 2005). Between 1.95 and 1.92 Ga, the Yinshan and Ordos blocks collided along the Khondalite belt to form the Western Block (e.g., Li et al., 2011; Lu et al., 2008; Zhao et al., 2005). Around 1.9 Ga, the Longgang and Nangrim blocks amalgamated along the Jiao-Liao-Ji belt, forming the Eastern Block (e.g., Luo et al., 2004; Zhao et al., 2005). The NCC ultimately formed by the assembly of the Eastern and Western Blocks along the central orogenic belt at *c.* 1.85 Ga (e.g., Zhao and Zhai, 2013; Zhao et al., 2000a, b, 2005). The southern margin of the NCC is separated from the North Qinling Orogen by the Luonan-Luanchuan Fault (Fig. 1b). Prior to the Mesozoic, the southern margin of the NCC has been the locus of tectonic activity. Therefore, this region is outstanding for studying the Precambrian geological evolution (e.g., Zhai, 2010).

The study area is located within the eastern part of the southern margin of the NCC (Fig. 1b). The most frequent rocks in this area are metamorphic basement rocks of the Archean Taihua Group. The Taihua Group extends in an east-west direction from Lantian in the west to Wuyang in the east (e.g., Diwu et al., 2014, 2018; Wang et al., 2020). It is primarily composed of medium- to high-grade metamorphic rocks and has been divided into the Lower and Upper Taihua Complex (e.g., Kröner et al., 1988;

105 Shen, 1994; Wan et al., 2006; Xue et al., 1995; Zhang et al., 1985). The Lower Taihua
106 Complex is dominated by metamorphic mafic rocks and TTG gneisses (e.g., Kröner et
107 al., 1988; Zhang et al., 1985), whereas the Upper Taihua Complex is characterized by
108 supracrustal sequences and metamorphic mafic rocks (e.g., Wan et al., 2006; Xue et
109 al., 1995). Rocks of the Taihua Group record two significant stages of Archean crustal
110 growth (e.g., Diwu et al., 2014, 2018). During the late Paleoproterozoic (1.97–1.80
111 Ga), the Taihua Group underwent widespread amphibolite to granulite facies
112 metamorphism and intense deformation, reflecting collisional processes in the NCC
113 (e.g., Diwu et al., 2018; Sun et al., 2017).

114 The upper part of the basement contains 1780-million-year-old volcanic rocks of the
115 Xiong'er Group (e.g., Zhao et al., 2004, 2007). The Xiong'er volcanic rocks consist
116 mainly of basalts and andesites that are widely distributed along the southern margin
117 of the NCC, and extend as far north as Taiyuan City in Shanxi Province (Zhao et al.,
118 2007). The Xiong'er Group represents the largest magmatic unit of the NCC since the
119 Neoarchean period. At the same time, a large mafic dyke swarm intruded into the
120 NCC. These mafic rocks are interpreted as products of crustal extension during the
121 Colombia supercontinent era (e.g., Hou et al., 2008; Peng et al., 2008).

122 During fieldwork, seven diorite samples were collected from the Jiguanshan diorite on
123 the eastern side of the Jiguanshan hill (or the Jiguan Mountain), about 30 km south of
124 Ruyang County, Henan Province (Fig. 1c and Table S1). The Jiguanshan diorite forms
125 several east-west striking bodies that are cut by the Mesozoic Taishanmiao A-type
126 granite to the west. The Taishanmiao intrusion covers an area of *c.* 290 km^2 (e.g., He

et al., 2021). The northern and eastern part of the Taishanmiao intrusion penetrates the volcanic rocks of the Xiong'er Group (Fig. 1c).

The collected rock samples of the Jiguanshan diorite are fresh and greyish with massive textures (Fig. 2a). They are fine-grained with grain sizes between 0.1–2 mm (Fig. 2b). The main mineral is plagioclase (~60 vol.%), with lamellar or euhedral shape and variable grain size. Under the microscope, the partially sericitized crystals show simple contact twinning and polysynthetic twinning. Some plagioclase crystals show zonal and resorption textures (Figs. 2c-e) and Carlsbad-albite twinning (Fig. 2d). Clinopyroxene (~15 vol.%) formed earlier than plagioclase. Most of the clinopyroxenes have zonal texture (Fig. 2f). Euhedral opaque minerals (~3 vol.%), such as ilmenite, are often enclosed in clinopyroxene. Alkali-feldspar (~10 vol.%) shows hypidiomorphic to xenomorphic texture with imprints of kaolinization (Figs. 2c, e). The mineral occurs as K-feldspar and perthite. Quartz (~5 vol.%) occurs as an anhedral crystal. Biotite (~3 vol.%) shows xenomorphic texture or is altered into chloride (Figs. 2c, e). In addition, accessory minerals such as zircon and ilmenite account for about 3 vol.% (Fig. 2f).

3 Analytical methods

Whole rock major and elements: Seven fresh rock samples were grinded into powders to less than 200 mesh size. Major element composition of whole-rock samples was analyzed by X-ray fluorescence (XRF) at ALS Chemex (Guangzhou) by

using PANalytical PW2424 instrument. Trace element concentrations were determined using Agilent 7700 inductively coupled plasma mass spectrometry (ICP-MS) at the University of Science and Technology of China (USTC). Measured concentrations of the reference materials (GSR–1, BCR–2, and AGV–2) are within 10% of their recommended values and the analytical uncertainties are better than 5%.

Whole-rock Sr-Nd-Pb isotopes: Whole-rock Sr-Nd-Pb isotope analysis was performed in the Laboratory of Radiogenic Isotope Geochemistry, USTC. *C.* 100 mg whole-rock powders were decomposed in purified HF and HNO_3 acid solution for Pb isotopic analysis and purified HF and $HClO_4$ acid solution for Sr-Nd isotopic analysis. Sr and Nd were separated by an AG 50W-X12 resin (200–400 mesh size) and purified using the Sr-Spec® ion-exchange resin for Sr and LN-Spec® resin for Nd. All isotopic measurements were measured on a Triton Plus mass spectrometer of Thermo Scientific™. Sr and Nd ratios were normalized to $^{86}Sr/^{88}Sr = 0.1194$ and $^{143}Nd/^{144}Nd = 0.7219$, respectively. Pb isotope ratios were corrected for mass fractionation using a fractionation factor of 0.1% per atomic mass unit based on repeated measurements of reference material NIST NBS 981 (Wang et al., 2023b). Total procedure blanks for Sr, Nd, and Pb were less than 200 pg. Detailed analytical procedures were described in Chen et al. (2000, 2007). Errors for the initial Sr and Nd isotope ratios were obtained by the error transfer formula, which is shown in Table 2 for Sr and Table 3 for Nd. Detailed formulas can be found in Siebel et al. (2005). A 5% age error, a 2‰ $^{87}Rb/^{86}Sr$ measurement error, and a 0.3‰ $^{87}Sr/^{86}Sr$ measurement error were used as uncertainties for the initial Sr value calculation. A 5% age error, a 0.3‰ $^{147}Sm/^{143}Nd$

error, and the $^{143}Nd/^{144}Nd$ measurement error were used for calculating the initial Nd isotope uncertainty.

Zircon U-Pb geochronology and trace element composition: Zircon crystals were separated from the rock samples by standard mineral separation procedures. Grains with intact crystal shape and no obvious inclusions were selected and embedded in epoxy resin under a binocular microscope. Most of the zircon gains were polished to half to two thirds of their original thickness and then cleaned in ultra-pure water by ultrasonic waves. Cathodoluminescence (CL) image analysis was done on a scanning electron microscope (SEM) at the USTC. Zircon U-Pb isotopic and trace element compositions were obtained by laser-ablation inductively-coupled plasma mass spectrometry (LA-ICP-MS) at the USTC. The beam spot diameter was 32 μm, operating at a repetition rate of 10 Hz. Helium served as the carrier gas. Zircon 91500 was used as a standard for age calculation. The NIST SRM 610 and 612 were utilized as reference materials for element content adjustment. U-Pb ratios and uranium and lead concentration data were calculated by the ICPMSDataCal software (Liu et al., 2010). Concordia and weighted mean age plots were made using IsoplotR (Vermeesch, 2018).

4 Analytical results

Whole-rock compositions of the Jiguanshan diorite are given in Table 1, and Sr-Nd-Pb isotope compositions and error calculations are shown in Tables 2 to 4. Age

191 results of zircon grains from four samples are given in Table S1, zircon trace element
192 composition in Table S2.

193

194 **4.1 Zircon U–Pb isotopic ages**

195 Zircon grains from the Jiguanshan diorite are transparent to pale yellow with
196 subhedral to euhedral habitus. They measure *c.* 100–300 μm in length and have aspect
197 ratios between 1:1 and 3:1. Most of them show oscillatory zoning in the CL images
198 (Fig. 3), which suggests a magmatic origin.

199 Twenty-nine zircon grains from sample ZY2202 yield $^{207}Pb/^{206}Pb$ ages varying from
200 1885 ±44 Ma to 1643 ±42 Ma giving a weighted mean age of 1772 ±16 Ma (2σ, n=29,
201 MSWD=2.2, Fig. 4a). Thirty-two zircon grains from sample ZY2204 yield $^{207}Pb/^{206}Pb$
202 ages varying from 1902 ±54 Ma to 1635 ±47 Ma with a weighted mean age of 1742
203 ±15 Ma (2σ, n=32, MSWD=1.6, Fig. 4b). Twenty-six out of twenty-seven zircon
204 grains from sample ZY2205 yield $^{207}Pb/^{206}Pb$ ages varying from 1933 ±52 Ma to
205 1692 ±44 Ma and a weighted mean age of 1760 ±18 Ma (2σ, n=26, MSWD=0.66, Fig.
206 4c). One zircon with a $^{207}Pb/^{206}Pb$ age of 1639 ±46 Ma (96% concordance) was
207 excluded from the calculation after being identified as a statistical outlier by the
208 IsoplotR program (Fig. 4c). The limited number of zircon grains of this age precludes
209 a robust geological interpretation. Thirty zircon grains of sample ZY2207 yield
210 $^{207}Pb/^{206}Pb$ ages ranging from 1900 ±54 Ma to 1700 ±36 Ma with a weighted mean
211 age of 1771 ±17 Ma (2σ, n=30, MSWD=1, Fig. 4d).

Most zircon grains have Th/U ratios >1, supporting their magmatic origin (Table S1). Some grains deviate from the Concordia curve, which is related to lead loss events or radiation damage (Fig. 4a-d). The weighted mean age of the Jiguanshan diorite of *c.* 1780 Ma suggests that the diorite body formed in the late Paleoproterozoic.

4.2 Whole-rock geochemical composition

SiO_2 contents of the Jiguanshan diorite vary between 55.57 and 59.44 wt. % and the sum of K_2O+Na_2O from 5.57 to 6.03 wt. %, corresponding to gabbroic diorite to diorite composition according to the TAS diagram (Fig. 5a). K_2O contents range from 2.97 to 3.21 wt. % and fall within the high-K calc-alkaline fields (Fig. 5b). The samples from the Jiguanshan diorite have consistent A/CNK ratios ranging from 0.78 to 0.81 and A/NK >1, which classify them as metaluminous rocks (Fig. 5c). $Mg^{\#}$ ($Mg^{\#}$=(MgO+FeO_{total})/MgO×100) values range from 34 to 39 (Fig. 5d).

The Jiguanshan diorite depicts enrichment in large ion lithophile elements (LILE), such as Rb, Ba, and K, and negative anomalies of Sr, Ti, Nb, and Ta (Fig. 6a). ∑REE contents range from 361 to 393 ppm. Light rare earth elements (LREE) exhibit stronger enrichment, while heavy rare earth elements (HREE) are relatively depleted (Fig. 6b). $(La/Yb)_N$ ratios range from 12.2 to 15.0 (subscript N denotes normalization against chondrite La and Yb contents) with Eu/Eu^* ($Eu/Eu^* = 2Eu_N/(Sm_N+Gd_N)$, subscript N denotes normalization against chondrite Sm and Gd contents) ratios ranging from 0.57 to 0.68 (Table 1).

4.3 Whole-rock Sr-Nd-Pb isotope compositions

All initial radiogenic isotope values and the errors of the initial Sr, Nd and Pb isotope ratios reported herein are calculated back to an age of 1780 Ma. The measured $^{87}Sr/^{86}Sr$ ratios for the Jiguanshan diorites vary from 0.715177 ±0.000011 to 0.724714 ±0.000012 (2σ). Initial Sr ratios range from 0.7020 ±0.0007 to 0.7058 ±0.0010 (2σ, Fig. 7a). Measured $^{143}Nd/^{144}Nd$ values vary from 0.511129 ±0.000008 to 0.511329 ±0.000007 (2σ). Initial $^{143}Nd/^{144}Nd$ isotope compositions range from 0.509924 ±0.000061 to 0.510090 ±0.000063 (2σ), corresponding to initial ε_{Nd} values of -8.04 ±1.20 to -4.80 ±1.23 (2σ, Fig. 7b) and two-stage Nd model ages (T_{DM2}) of 2.94 Ga to 2.68 Ga. Pb isotopic compositions are as follows: $^{206}Pb/^{204}Pb$ = 15.832–16.167, $^{207}Pb/^{204}Pb$ = 15.170–15.243, and $^{208}Pb/^{204}Pb$ = 36.046–37.324. Initial Pb isotope ratios are significantly lower: $^{206}Pb/^{204}Pb_i$ ratios ranging from 14.965 to 15.295, $^{207}Pb/^{204}Pb_i$ ratios ranging from 15.090 to 15.150, $^{208}Pb/^{204}Pb_i$ ratios ranging from 34.398 to 35.825, with $^{238}U/^{204}Pb$ and $^{232}Th/^{238}U$ ratios ranging from 2.3 to 2.9 and 5.3 to 7.8, respectively (Fig. 8).

5 Discussion

5.1 Composition of late-Paleoproterozoic diorites of the NCC

On a regional scale, the late Paleoproterozoic diorites of the NCC are distributed in a roughly east to west direction, unlike the north-northwest (NNW) strike, that

characterizes the contemporaneous mafic dykes (Hou et al., 2008; Peng et al., 2007, 2008). Intrusion ages of the diorites are concentrated between 1780 and 1750 Ma. All diorites have similar geochemical and isotopic compositions and can be regarded as a compositional homogeneous rock group.

Most of the late-Paleoproterozoic diorites of the NCC have silica contents in the range of 52-62 wt. % (Fig. 5a). Total alkali content (K_2O+Na_2O) of 5-7 wt. % suggests a subalkaline character (Fig. 5a). K_2O contents range from 2-5 wt. % in accordance with a high-K calc-alkaline to shoshonite composition (Fig. 5b). The ASI and $Mg^{\#}$ values of the samples, except for a few data points that deviate significantly, are mostly homogeneous, with weighted average values of 0.81 and 37, respectively (Figs. 5c, d). In primitive mantle normalization multi-element diagrams, all diorites display enrichment of LILEs, such as Rb, Ba, and K, and depletion of high field strength elements (HFSEs), such as Na, Ta, Th, U, and Ti (Fig. 6). On the rare earth element normalization diagrams, they display negative Eu anomalies with enrichment in LREEs and a flat pattern of HREEs (Fig. 6).

All diorites have similar Nd isotopic compositions with a mean initial ε_{Nd} value of -6.5 ±0.2 (2σ, n=41, Fig. 7b) . The overall range of initial ε_{Nd} values is from -10.2 ±1.2 to -4.8 ±1.2 (2σ, Fig. 7b). Some samples from the Wafang diorite (or Muzhijie diorite, Ma et al, 2023b; Wang et al, 2016) have enriched Nd isotope composition, which can be explained by assimilation or contamination of continental crust due to their higher zirconium content (Fig. 7b; Table 3). Overall, the initial ε_{Nd} values and the corresponding two-stage Nd model ages (T_{DM2}) of the diorites are consistent with

each other except for the Wafang diorite (Table 3).

Initial ε_{Hf} values of zircons from the diorites in the NCC show a wide but consistent range of variations, i.e., from -17 to -2.5 in the Gushicun diorite (Ma et al, 2023a; Fig. 7c), from -14 to 0.55 in the Muzhijie diorite (Ma et al, 2023b; Fig. 7c), and from -17 to 0.95 in the Fudian diorite (Ma et al., 2023b; Fig. 7c). The diorites have similar Nd-Hf isotopic compositions and form a coherent group in geochemical diagrams, indicating a close genetic relationship.

5.2 Initial Sr isotope composition and magma source characteristics

The late Paleoproterozoic diorites of the NCC show a large range in whole-rock initial Sr isotope composition (Fig. 7a). Determining magma sources for rocks with widely varying initial Sr ratios is complex, as Sr isotopes can be affected by magma mixing, assimilation, contamination, and melting degrees (e.g., Gao et al., 2015; Wolf et al., 2019; Zeng et al., 2005).

The whole-rock Nd and Sr isotope composition of the diorites suggest a heterogeneous magma source (Fig. 7d). It might be argued that this could be the effect of mixing between crustal and mantle sources. However, mantle-derived rocks often have high MgO contents and elevated compatible element concentrations such as Ni and Cr, which is inconsistent with the element characteristics of the diorites (Table 1, see previous references). Variability in Sr isotope ratios can result from different degrees of source melting. However, a mica- and feldspar-rich source with high Rb/Sr

297 ratios can produce melts with more radiogenic $^{87}Sr/^{86}Sr$ ratios (e.g., Hu et al., 2018).
298 Melts affected by dehydration of amphibole typically have low $^{87}Sr/^{86}Sr$ ratios and
299 adakitic characteristics (e.g., Rapp and Watson, 1995; Wolf et al., 1993). Thus,
300 different degrees of source melting are unlikely to be the main cause for the isotopic
301 composition of the diorites.

302 Initial $^{87}Sr/^{86}Sr$ ratios <0.704 are negatively correlated with the $^{87}Rb/^{86}Sr$ ratios (Fig.
303 7a). For initial $^{87}Sr/^{86}Sr$ ratios >0.704, such correlation does no longer exist. A reason
304 for this could be the large uncertainty propagation of the initial whole-rock Sr isotope
305 ratios especially for old samples. Among all diorites there are samples with initial
306 $^{87}Sr/^{86}Sr$ ratios >0.704. Excluding outliers, the mean average initial $^{87}Sr/^{86}Sr$ ratio is
307 0.7052 ±0.0003 (2σ, n=8), which might represent the initial Sr isotope composition of
308 the magma source (Fig. 7a).

309 The initial Sr ratios of the Xiong'er Group rocks vary widely and tend to be more
310 radiogenic compared to the diorites (Fig. 7d). The initial Sr ratios of the diorites are
311 more similar to lower crustal Archean xenoliths from the southeastern NCC (initial
312 $^{87}Sr/^{86}Sr$ ratios: 0.7039–0.7068, t=1780 Ma, e.g., Huang et al., 2004), suggesting that
313 they are more likely associated with lower crustal rocks of the NCC rather than an
314 enriched mantle source like the volcanic rocks of the Xiong'er Group.

315

316 **5.3 Petrogenesis of the dioritic rocks**

317 Several models have been proposed for the petrogenesis of intermediate dioritic rocks

including partial melting of metasomatized mantle (e.g., Chen et al., 2021), partial melting of subducted oceanic crust and subsequent melt-peridotite reaction (e.g., Kelemen, 1995; Stern and Kilian, 1996), magma mixing/mingling (e.g., Reubi and Blundy, 2009; Streck et al., 2007), melting of basaltic rocks (e.g., Jackson et al., 2003; Petford and Atherton, 1996), as well as fractional crystallization of basaltic magmas (e.g., Castillo et al., 1999).

The diorites from the NCC have low compatible element concentrations, suggesting that they were not derived directly from a mantle source (Fig. 9a). Larger contribution of mantle material can also be excluded due to their initial Nd isotope features (Fig. 7b), silica and $Mg^{\#}$ values (Fig. 5d).

Partial melting of subducting oceanic crust can also form rocks of intermediate composition, such as adakites, which often exhibit high Sr/Y ratios (>20) and low Y contents (<18 ppm) (e.g., Defant and Drummond, 1990; Peacock et al., 1994). The Jiguanshan and other diorites from the NCC have relatively high Y and Sr contents with Sr/Y ratios <15. Thus, partial melting of oceanic crust does not appear to have played a role during the genesis of the diorites.

Cr contents decrease with decreasing MgO, indicating fractionation of clinopyroxene (Fig. 9a). CaO contents decrease with increasing SiO_2, suggesting crystallization of minerals, such as plagioclase or clinopyroxene (Fig. 9b). However, Al_2O_3 and Na_2O contents do not significantly decrease with increasing SiO_2, indicating that plagioclase and clinopyroxene were not significant fractionation phases (Figs. 9c-d). The increase

in K_2O contents with increasing SiO_2 suggests no biotite and/or K-feldspar fractionation during magmatic evolution (Fig. 9e). Increasing SiO_2 and decreasing TiO_2 indicate crystallization and fractionation of Ti-bearing minerals, such as ilmenite (Fig 9f). Eu/Eu^* values of the diorites do not show significant changes with Sr contents, which provides evidence that fractionation of plagioclase from the melt was not significant (Fig. 9g).

From the above discussion, it can be concluded that the petrogenesis of the diorites in the NCC was associated with minor fractional crystallization processes. Whole-rock La/Yb versus La and Zr/Sm versus Zr correlations are as expected for a partial melting process (Figs. 9h-i). This implies that the formation of the diorites may be closely related to the partial melting of a basaltic protolith.

Basement rocks of the lower Taihua Group at the southern margin of the NCC consist of amphibolite (e.g., Diwu et al., 2014, 2018; Wang et al., 2020). Partial melting of amphibolite can lead to the production of intermediate to acidic magmas (e.g., Beard and Lofgren, 1991; Rapp and Watson, 1995). The amphibolites of the Taihua Group are characterized by low K content and low K_2O/Na_2O ratios (<0.5, Wang et al., 2019), making it difficult to generate high-K_2O rocks. (Beard and Lofgren, 1991; Roberts and Clemens, 1993). Partial melting of amphibolite typically results in the formation of peraluminous melts (e.g., Beard and Lofgren, 1991; Rapp and Watson, 1995), whereas the diorites in the NCC have low Al_2O_3 content and metaluminous character (Fig. 5c; Weighted average A/NCK values of 0.81). Additionally, the ε_{Nd} values of the Taihua Group amphibolites at t=1780 Ma vary widely from -6.7 to 0.4,

different from those of the diorites (Wang et al., 2019). Therefore, it seems unlikely that the diorites formed by the partial melting of Taihua Group amphibolites.

Mafic rocks of the Xiong'er Group and mafic dyke swarms were argued to be the source of the diorites (Cui et al., 2011; Ma et al., 2023b; Peng et al., 2007). Such rocks possess a relatively large range of initial Sr and Nd isotopic compositions (Fig. 7d), while the initial Nd isotopic compositions of the diorites are relatively homogeneous (Fig. 7b). Whole-rock initial Nd ratios and zircon initial Hf isotope ratios of the Xiong'er Group rocks are also enriched (Fig. 7c). Initial Pb isotopic compositions of the mafic dykes and Xiong'er Group rocks are very radiogenic and variable (Figs. 8a, b), which is due to the high U and Th contents of the protolith, indicating the presence of an enriched subcontinental lithospheric mantle source (e.g., Hou et al., 2008; Peng et al., 2004, 2007; Wang et al., 2004, 2010; Zhao et al., 2007). Based on the previous discussion, the geochemical characteristics of the diorites are more compatible with a crustal origin and the isotopic compositions of the diorites indicate that they were not derived from an enriched mantle source.

Additionally, the Xiong'er volcanic rocks have lower Nb/Ta ratios and Nb contents compared to the diorites (Fig. 10a). Nb and Ta share a similar valence state and atomic radii, but they can undergo fractionation during the subduction process (Jochum et al., 1986; Shannon, 1976). The Xiong'er volcanic rocks, with higher and positively correlated Ba/Th and Sr/Th ratios (Figs. 10a-b), likely originated from a source influenced by an early subduction component, whereas the diorites appear to be less affected by early subduction-related materials. Therefore, it seems likely that

the diorites were formed by partial melting of a mafic lower crustal protolith on top of an enriched subcontinental lithospheric mantle beneath the NCC.

5.4 Tectonic implications

After Paleoproterozoic collision and amalgamation, the NCC was intruded by diverse magmatic rocks, which have been interpreted as products of continental arc magmatism, post-collisional extension, or continental rift/mantle plume magmatism.

The volcanic rocks of the Xiong'er Group along the southern margin of the NCC are dominated by andesites, exhibiting calc-alkaline characteristics and negative Nb-Ta-Ti anomalies (Jia, 1987, He et al., 2009; Zhao et al., 2009). These signatures together with Nd isotope evidence for ancient crustal assimilation and multiphase volcanic activities, support a continental arc environment for the formation of the Xiong'er Group (He et al., 2009; Zhao et al., 2009).

The radially distributed mafic dike swarms, accompanied by A-type granite intrusions and rift-related sedimentary sequences, are indicative of a continental rift setting (e.g., Fan et al., 2024; Xu et al., 2008; Zhao et al., 2002; Zhao et al., 2002, 2007). The Xiong'er Group is dominated by andesites, dacites, and rhyolites with minor basaltic andesites, which some researchers interpret as an atypical bimodal suite suggestive of a continental rift setting (Zhao et al., 2002, 2007). Furthermore, the 1.80 to 1.75 Ga old mafic dike swarms are distributed in a radial or concentric pattern centered on the Xiong'er Rift and extending northward (Peng et al., 2007). They share geochemical

characteristics, such as high TiO_2 and MgO contents, enrichment in LREEs, Ba, and K, and depletion in Nb-Ta which is interpreted as evidence for lithospheric extension induced by mantle plume upwelling (e.g., Hou et al., 2008; Peng et al., 2007, 2008).

The post-collisional extension model emphasizes that the late Paleoproterozoic magmatism occurred during lithospheric delamination and possibly slab detachment (e.g., Wang et al., 2004, 2008, 2014, 2023a). The mafic dikes are enriched in LILEs and LREEs but depleted in HFSEs, and show negative $\varepsilon_{Nd}(t)$ and $\varepsilon_{Hf}(t)$ values. This suggests derivation from an enriched lithospheric mantle previously metasomatized by subduction zone fluids (e.g., Hu et al., 2010; Wang et al., 2004, 2008, 2014). The dikes are concentrated in the Trans-North China Orogen and nearby areas, consistent with extensional fractures caused by a rising asthenosphere (Wang et al., 2004, 2008, 2014). Their geochemical features, lacking OIB or asthenospheric mantle affinities, do not support a mantle plume origin (Wang et al., 2014).

Calk-alkaline diorites are important intermediate rock that typically form at island arcs, subduction zones, and continental collision orogenic belts along convergent plate boundaries. Island arc intermediate rocks, such as boninites and andesites are generally characterized by high MgO, Cr, and Ni contents (Hickey et al., 1982; Rapp and Watson, 1995), whereas continental arc intermediate rocks typically show high Al_2O_3 content with a wider range of $^{87}Sr/^{86}Sr$ and $^{143}Nd/^{144}Nd$ isotope compositions, reflecting an obvious influence of continental crust or more enriched sources (Hawkesworth et al., 1979; Peacock et al., 1994). The Paleoproterozoic diorites of the NCC lack the compositional features of arc-related rocks, meanwhile, their trace

element distributions differ from those of island arc and continental arc intermediate rocks. For example, the diorites do not show significant enrichment in Sr, Th, and U compared to arc-related rocks (Fig. 6a). The diorites also exhibit a negative Eu anomaly in the REE diagram, which is different from arc-related rocks (Fig. 6b). Diorites in collisional orogenic belts have high MgO and K_2O contents and adakite-like characteristics with high Sr/Y and La/Yb ratios (Yang et al., 2015). However, Paleoproterozoic diorites of the NCC do not show typical arc-related element and isotopic signatures, suggesting formation in a non-subduction environment.

Diorites can also form during crustal extension (Asmerom et al., 1990; Liu et al., 2024). The NCC was in a post-collisional extensional setting after its final amalgamation (e.g., Zhai, 2010). During this stage, magmatism becomes more complex (Bonin, 2004). Zircon is a very stable mineral and its trace elements offer significant potential for distinguishing between different tectonic settings. For the following discussion, zircon samples with La contents (< 1 ppm) were selected to ensure accurate information from zircon trace element contents without interference from the inclusion of other accessory phases (Zou et al., 2019). All zircons from the diorites plot within the continental area in the U/Yb versus Y diagram (Fig. 11a), and most of them fall into a rift-controlled tectonic environment in tectonic discrimination diagrams (Figs. 11b, c; Carly et al., 2014).

Furthermore, HFSE elements, such as Zr, Nb, Ta, Hf, and Th, are important tectonic indices. The distinctive Th content in arc magmas is primarily due to its low solubility

448 in subduction zone fluids and its contribution from sedimentary components (e.g.,
449 Bailey and Ragnasdottir, 1994; Pearce and Peate, 1995). Arc-related/orogenic
450 magmas usually have less Nb than those of within-plate settings (e.g., Pearce and
451 Peate, 1995; Sun and McDonough, 1989). Nb in zircon is thought to be incorporated
452 through xenotime-type substitution (Schulz et al., 2006) and is suggested to reflect the
453 magma composition with minimal influence of magmatic fractionation (Hoskin et al.,
454 2000; Schulz et al., 2006). In the Nb/Hf versus Th/U and Hf/Th versus Th/Nb
455 diagrams, zircons from the Fudian and Gushicun diorites plot within or close to the
456 arc-related/orogenic area (Figs. 11d, e). The Jiuganshan and Muzhijie diorites plot in
457 the arc-related/orogenic and within-plate/anorogenic areas (Figs. 11d, e). Whole-rock
458 Ta/Yb and Th/Yb ratios of the diorites are uniform (Fig. 11f), all falling within the
459 overlapping area of the ACM (active continental margins) and WPVZ (within-plate
460 volcanic zone). This may indicate that the post-collisional extension during this period
461 proceeded continuously and progressively into a rift evolution. Nevertheless, the
462 diorites preserve a record of superposition of components from multiple tectonic
463 settings.

464 After the ~1.85 Ga collisional event, the NCC entered into a prolonged
465 post-collisional extensional stage (Fig. 12). During this stage, magmatism was
466 primarily controlled by crustal thickening and remelting, leading to the widespread
467 formation of various crust-derived granites (e.g., Geng et al., 2006; Zhao et al., 2008,
468 2018). Subsequent slab breakoff and gravitational collapse of the thickened crust
469 triggered extension in the mid-upper crust and emplacement of felsic magmas (Deng

et al., 2016a; Wang et al., 2023a; Xu et al., 2024). At *c.* 1.78 Ga, lithospheric thinning induced upwelling of the asthenosphere, causing further partial melting of previously subduction-fluid-metasomatized lithospheric mantle (e.g., Peng et al., 2007, 2008; Wang et al., 2010, 2014; Zhao et al., 2002, 2007). Following this event, the magmatic activity in this region became dominated by A-type granites and alkaline rocks, marking a transition to an anorogenic intracontinental extensional setting (e.g., Deng et al., 2016b; Wang et al., 2024). The 1.78 Ga old crust-derived diorites show transitional geochemical features, retaining some remnant effects of orogenic magmatism while gradually evolving toward intraplate magmatism. It reflects the ongoing extension of the NCC after its amalgamation.

6 Conclusions

The Jiguanshan diorite yields a U-Pb zircon age of *c.* 1.78 Ga. The intrusion displays geochemical features in common with other Paleoproterozoic diorite intrusions of the NCC. The diorite emplaced contemporaneous with the Xiong'er volcanic rocks and the mafic dyke swarms, representing a significant period of magmatism in the NCC.

The diorites were produced by partial melting of a mafic protolith. The Sr-Nd-Pb-Hf isotopic characteristics indicate that the source was not the same as that for the Xiong'er volcanic rocks or the mafic dyke swarms. Instead, the diorites were likely derived from the lower crust of the NCC.

The formation of Paleoproterozoic diorites in the NCC was not connected with arc

magmatism. Instead, it was associated with a rift setting. The formation of diorite records the transition of crustal origin rocks from orogenic-related magmatism to intraplate magmatism during the post-collision extensional stage. It therefore reflects the ongoing extension of the NCC after its amalgamation.

Acknowledgements

This study was financially supported by the Strategic Priority Research Program of the Chinese Academy of Sciences (grant Nos. XDA0430203) and the National Natural Science Foundation of China (grant Nos. 42202069 and 41872049). Zhiyi Wang was financially supported by China Scholarship Council (202306340065). We thank P. Xiao and Z.-H. Hou for assistance during analysis.

Author contributions

Zhiyi Wang: Investigation, Writing - Review & Editing; Jun He & Fukun Chen: Supervision, Writing - Review & Editing, Funding acquisition; Wolfgang Siebel: Conceptualization, Writing - Review & Editing; Shuhao Tang, Yiru Ji, Jianfeng He: Data collection for this paper.

Conflict of interest:

The authors declare no competing financial and non-financial interests for this study.

References

Asmerom, Y., Snow, J. K., Holm, D. K., Jacobsen, S. B., Wernicke, B. P., and Lux, D. R.: Rapid uplift and crustal growth in extensional environments: An isotopic study from the Death Valley region, California. Geology, 18, 223–226. https://doi.org/10.1130/0091-7613(1990)018<0223:RUACGI>2.3.CO;2, 1990.

Bailey, E.H., and Ragnarsdottir, K.V.: Uranium and thorium solubilities in subduction zone fluids. Earth Planet. Sci. Lett., 124, 119–129. https://doi.org/10.1016/0012-821X(94)00071-9, 1994.

Beard, J.S., and Lofgren, G.E.: Dehydration melting and water-saturated melting of basaltic and andesitic greenstones and amphibolites at 1, 3, and 6.9 kb. J. Petrol. 32, 365-401. https://doi.org/10.1093/petrology/32.2.365, 1991.

BGMRH (Bureau of Geology and Mineral Resources of Henan Province): Geological map of the Henan Province. Sheet I-49-(23) (Lushan) scale 1:200,000 (in Chinese), 1994.

Bonin, B.: Do coeval mafic and felsic magmas in post-collisional to within-plate regimes necessarily imply two contrasting, mantle and crustal sources? A review. Lithos, 78, 1–24. https://doi.org/10.1016/j.lithos.2004.04.042, 2004.

Carley, T.L., Miller, C.F., Wooden, J.L., Padilla, A.J., Schmitt, A.K., Economos, R.C., Bindeman, I.N., and Jordan, B.T.: Iceland is not a magmatic analog for the Hadean: evidence from the zircon record. Earth Planet. Sci. Lett., 405, 85-97. https://doi.org/10.1016/j.epsl.2014.08.015, 2014.

Castillo, P., Janney, P., and Solidum, R.: Petrology and geochemistry of Camiguin Island, southern Philippines: insights to the source of adakites and other lavas in a complex arc setting. Contrib. Mineral. Petrol., 134, 33–51. https://doi.org/10.1007/s004100050467, 1999.

Chen, F., Hegner, E., and Todt, W.: Zircon ages, Nd isotopic and chemical compositions of orthogneisses from the Black Forest, Germany - evidence for a Cambrian magmatic arc. Int. J. Earth Sci., 88, 791-802. https://doi.org/10.1007/s005310050306, 2000.

538 Chen, F., Li, X. H., Wang, X. L., Li, Q. L., and Siebel, W.: Zircon age and Nd-Hf isotopic composition
539 of the Yunnan Tethyan belt, southwestern China. Int. J. Earth Sci., 96, 1179-1194.
540 https://doi.org/10.1007/s00531-006-0146-y, 2007.

541 Chen, L., Zheng, Y.F., Xu, Z., and Zhao, Z.F.: Generation of andesite through partial melting of basaltic
542 metasomatites in the mantle wedge: Insight from quantitative study of Andean andesites. Geosci.
543 Front., 12, 101124. https://doi.org/10.1016/j.gsf.2020.12.005, 2021.

544 Cui, M.L., Zhang, B.L., Peng, P., Zhang, L.C., Shen, X.L., Guo, Z.H., and Huang, X.F.:
545 Zircon/baddeleyite U-Pb dating for the Paleoproterozoic intermediate-acid intrusive rocks in
546 Xiaoshan Mountains, west of Henan Province and their constraints on the age of the Xiong'er
547 Volcanic Province. Acta Petrol. Sin. (in Chinese with English abstract), 26, 1541-1549, 2010.

548 Cui, M.L., Zhang, B.L., and Zhang, L.C.: U–Pb dating of baddeleyite and zircon from the Shizhaigou
549 diorite in the southern margin of North China Craton: Constraints on the timing and tectonic setting
550 of the Paleoproterozoic Xiong'er group. Gondwana Res., 20, 184-193.
551 https://doi.org/10.1016/j.gr.2011.01.010, 2011.

552 Defant, M., and Drummond, M.: Derivation of some modern arc magmas by melting of young
553 subducted lithosphere. Nature, 347, 662-665. https://doi.org/10.1038/347662a0, 1990.

554 Deng, X. Q., Peng, T. P., and Zhao, T. P.: Geochronology and Geochemistry of the Late
555 Paleoproterozoic Aluminous A-Type Granite in the Xiaoqinling Area along the Southern Margin of
556 the North China Craton: Petrogenesis and Tectonic Implications. Precambrian Res., 285: 127–146.
557 https://doi.org/10.1016/j.precamres.2016.09.013, 2016a

558 Deng, X.Q., Zhao, T.P., and Peng, T.P.: Age and geochemistry of the early Mesoproterozoic A-type
559 granites in the southern margin of the North China Craton: Constraints on their petrogenesis and
560 tectonic implications, Precambrian Research, 283, 68–88,
561 https://doi.org/10.1016/j.precamres.2016.07.018, 2016b.

562 Diwu, C.R., Liu, X., and Sun, Y.: The composition and evolution of the Taihua Complex in the
563 southern North China Craton. Acta Petrol. Sin. (in Chinese with English abstract), 34, 999–1018,
564 2018.

565 Diwu, C.R., Sun, Y., Zhao, Y., and Lai, S.C.: Early Paleoproterozoic (2.45–2.20 Ga) magmatic activity
566 during the period of global magmatic shutdown: Implications for the crustal evolution of the
567 southern North China Craton. Precambrian Res., 255, 627-640.
568 https://doi.org/10.1016/j.precamres.2014.08.001, 2014.

569 Fan, Y. H., Zhu, X. Y., Duan, Q. S., Ma, J. F., Jia, C. Y., Liu, S. Q., and Zhao, T. P.: Discovery of 1.79
570 Ga dacite porphyry in the Taiyueshan Mts: Constraints on the genesis of the southern rift system in
571 the North China Craton, Acta Petrologica Sinica (in Chinese with English abstract), 40(4), 1327–
572 1342, https://doi.org/10.18654/1000-0569/2024.04.17, 2024.

573 Gao, J.F., Zhou, M.F., Robinson, P.T., Wang, C.Y., Zhao, J.H., and Malpas, J.: Magma mixing recorded
574 by Sr isotopes of plagioclase from dacites of the Quaternary Tengchong volcanic field, SE Tibetan
575 Plateau. J. Asian Earth Sci., 98, 1-17. https://doi.org/10.1016/j.jseaes.2014.10.036, 2015.

576 Geng, Y.S., Du, L.L., and Ren, L.D.: Growth and reworking of the early Precambrian continental crust
577 in the North China Craton: Constraints from zircon Hf isotopes. Gondwana Res., 21, 517-529.
578 https://doi.org/10.1016/j.gr.2011.07.006, 2012.

579 Geng, Y. S., Yang, C. H., and Wan, Y. S.: Paleoproterozoic granitic magmatism in Lüliang area, North
580 China Craton: constraint from isotopic geochronology, Acta Petrologica Sinica (in Chinese with
581 English abstract), 22, 305–314, 2006.

582 Gorton, M.P., and Schandl, E.S.: From continents to island arcs: A geochemical index of tectonic
583 setting for arc-related and within-plate felsic to intermediate volcanic rocks. Can. Mineral., 38,
584 1065–1073. https://doi.org/10.2113/gscanmin.38.5.1065, 2000.

585 Grimes, C.B., John, B.E., Kelemen, P.B., Mazdab, F., Wooden, J.L., Cheadle, M.J., Hanghøj, K., and
586 Schwartz, J.J.: Trace element chemistry of zircons from oceanic crust: a method for distinguishing
587 detrital zircon provenance. Geology, 35, 643-646. https://doi.org/10.1130/G23603A.1, 2007.

588 Hawkesworth, C.J., Norry, M.J., Roddick, J.C., Baker, P.E., Francis, P.W., and Thorpe, R.S.:
589 143Nd/144Nd, 87Sr/86Sr, and incompatible element variations in calc-alkaline andesites and
590 plateau lavas from South Amer*ica.* Earth Planet. Sci. Lett., 42, 45–57.
591 https://doi.org/10.1016/0012-821X(79)90189-4, 1979.

592 Hawkesworth, C.J., and Kemp, A.I.S.: Using hafnium and oxygen isotopes in zircons to unravel the
593 record of crustal evolution. Chem. Geol., 226, 144-162.
594 https://doi.org/10.1016/j.chemgeo.2005.09.018, 2006.

595 He, J., Qi, Y., Fan, X., and Chen, F.: Petrogenesis of the Taishanmiao A-type granite in the eastern
596 Qinling orogenic belt: Implications for tectonic transition and mineralization in the Late Cretaceous.
597 J. Geol., 129, 97-114. https://doi.org/10.1086/713726, 2021.

598 He, Y.H., Zhao, G.C., Sun, M., and Wilde, S.A.: Geochemistry, isotope systematics and petrogenesis of
599 the volcanic rocks in the Zhongtiao Mountain: An alternative interpretation for the evolution of the
600 southern margin of the North China Craton. Lithos, 102, 158-178.
601 https://doi.org/10.1016/j.lithos.2007.09.004, 2008.

602 He, Y.H., Zhao, G.C., Sun, M., and Xia, X.: SHRIMP and LA-ICP-MS zircon geochronology of the
603 Xiong'er volcanic rocks: Implications for the Paleo-Mesoproterozoic evolution of the southern
604 margin of the North China Craton. Precambrian Res., 168, 213-222.
605 https://doi.org/10.1016/j.precamres.2008.09.011, 2009.

606 He, Y.H., Zhao, G.C., Sun, M., and Han, Y.G.: Petrogenesis and tectonic setting of volcanic rocks in the
607 Xiaoshan and Waifangshan areas along the southern margin of the North China Craton: Constraints
608 from bulk-rock geochemistry and Sr–Nd isotopic composition. Lithos, 114, 186-199.
609 https://doi.org/10.1016/j.lithos.2009.08.008, 2010.

610 Hickey, R.L., and Frey, F.A.: Geochemical characteristics of boninite series volcanics: implications for
611 their source. Geochim. Cosmochim. Acta, 46(11), 2099–2115.
612 https://doi.org/10.1016/0016-7037(82)90188-0, 1982.

613 Hou, G.T., Li, J.H., Yang, M.H., Yao, W.H., Wang, C.C., and Wang, Y.X.: Geochemical constraints on
614 the tectonic environment of the Late Paleoproterozoic mafic dyke swarms in the North China
615 Craton. Gondwana Res., 13, 103-116. https://doi.org/10.1016/j.gr.2007.06.005, 2008.

616 Hoskin, P.W.O., Kinny, P.D., Wyborn, D., and Chappell, B.W.: Identifying accessory mineral saturation
617 during differentiation in granitoid magmas: an integrated approach. J. Petrol., 41, 1365–1396.
618 https://doi.org/10.1093/petrology/41.9.1365, 2000.

619 Hu, G. H., Hu, J. L., Chen, W., and Zhao, T. P.: Geochemistry and tectonic setting of the 1.78 Ga mafic
620 dyke swarms in the Mt. Zhongtiao and Mt. Song areas, the southern margin of the North China
621 Craton, Acta Petrologica Sinica (in Chinese with English abstract), 26, 1563–1576, 2010.

622 Hu, G.Y., Zeng, L.S., Gao, L.E., Liu, Q.P., Chen, H., and Guo, Y.S.: Diverse magma sources for the
623 Himalayan leucogranites: Evidence from B-Sr-Nd isotopes. Lithos, 314-315, 88-99.
624 https://doi.org/10.1016/j.lithos.2018.05.022, 2018.

625 Huang, X.L., Xu, Y.G., and Liu, D.Y.: Geochronology, petrology and geochemistry of the granulite
626 xenoliths from Nushan, east China: implication for a heterogeneous lower crust beneath the
627 Sino-Korean Craton. Geochim. Cosmochim. Acta, 68, 127-149.
628 https://doi.org/10.1016/S0016-7037(03)00416-2, 2004.

629 Jackson, M.D., Cheadle, M.J., and Atherton, M.P.: Quantitative modeling of granitic melt generation
630 and segregation in the continental crust. J. Geophys. Res. Solid Earth, 108, 2332.
631 https://doi.org/10.1029/2001JB001050, 2003.

632 Jia, C.Z., Petro-geochemistry of volcanic rocks in the Xiong'er Group: implications for tectonic setting.
633 Henan Geol. 2:39–43 (in Chinese with English abstract), 1985.

634 Jochum, K.P., Seufert, H.M., Spettel, B., and Palme, H.: The solar-system abundances of Nb, Ta, and Y,
635 and the relative abundances of refractory lithophile elements in differentiated planetary bodies.
636 Geochim. Cosmochim. Acta, 50, 1173-1183. https://doi.org/10.1016/0016-7037(86)90400-X, 1986.

637 Kelemen, P.B.: Genesis of high $Mg^{\#}$ andesites and the continental crust. Contrib. Mineral. Petrol., 120,
638 1-19. https://doi.org/10.1007/BF00311004, 1995.

639 Kröner, A., Compston, W., Zhang, G.-W., Guo, A.-L., and Todt, W.: Age and tectonic setting of Late
640 Archean greenstone-gneiss terrain in Henan Province, China, as revealed by single-grain zircon
641 dating, Geology, 16, 211–215,
642 https://doi.org/10.1130/0091-7613(1988)016<0211:AATSOL>2.3.CO;2, 1988.

643 Le Bas, M.J., Le Maitre, R.W., Streckeisen, A., and Zanettin, B.: A Chemical Classification of
644 Volcanic-Rocks Based on the Total Alkali Silica Diagram. J. Petrol., 27, 745-750.
645 https://doi.org/10.1093/petrology/27.3.745, 1986.

Li, X. P., Yang, Z. Y., Zhao, G. C., Grapes, R., and Guo, J. H.: Geochronology of khondalite-series rocks of the Jining Complex: Confirmation of depositional age and tectonometamorphic evolution of the North China craton, Int. Geol. Rev., 53, 1194–1211, doi:10.1080/00206810903548984, 2011.

Liu, A.L., Hai, L.F., Liu, J.K., Zhang X.J., Li H.F., Zhao F.S., Zhao G.L., and Bai J.H.: Geochronology, Geochemistry, and Sr-Nd-Hf Isotopes of the Diorite Porphyrites from the Weining Beishan Area, Ningxia Hui Autonomous Region: Constraints on Their Source and Tectonic Implications. J. Earth Sci. 35, 462–475. https://doi.org/10.1007/s12583-021-1491-2, 2024.

Liu, D.Y., Nutman, A.P., Compston, W., Wu, J.S., and Shen, Q.H.: Remnants of ≥ 3800 Ma crust in the Chinese part of the Sino-Korean Craton. Geology, 20, 339-342. https://doi.org/10.1130/0091-7613(1992)020<0339:ROMCIT>2.3.CO;2, 1992.

Liu, Y.S., Hu, Z.C., Zong, K.Q., Gao, C.G., Gao, S., Xu, J.A., and Chen, H.H.: Reappraisement and refinement of zircon U-Pb isotope and trace element analyses by LA-ICP-MS. Chin. Sci. Bull. (in Chinese with English abstract), 1535-1546, 2010.

Lu, S.N., Zhao, G.C., Wang, H.C., and Hao, G.J.: Precambrian metamorphic basement and sedimentary cover of the North China Craton: A review. Precambrian Res., 160, 77–93, 2008.

Luo, Y., Sun, M., Zhao, G. C, Li, S.Z., Xu, P., Ye, K., and Xia, X.P.: LA-ICP-MS U–Pb zircon ages of the Liaohe Group in the Eastern Block of the North China Craton: constraints on the evolution of the Jiao-Liao-Ji Belt, Precambrian Research, 134(3-4), 349-371, https://doi.org/10.1016/j.precamres.2004.07.002, 2004.

Ma, J.F., Qu, C.H., Zhou, Y.Y., and Zhao, T.P.: The genesis of *ca.* 1.78 Ga granitoids in the Xiong'er large igneous province: Implications for continental crust generation. Geol. Soc. Am. Bull., 135, 3213-3227. https://doi.org/10.1130/B36694.1, 2023a.

Ma, J.F., Wang, X.L., Yang, A.Y., and Zhao, T.P.: Tracking crystal-melt segregation and accumulation in the intermediate magma reservoir. Geophys. Res. Lett., 50, e2022GL102540. https://doi.org/10.1029/2022GL102540, 2023b.

Maniar, P.D., and Piccoli, P.M.: Tectonic discrimination of granitoids. Geol. Soc. Am. Bull., 101, 635-643. https://doi.org/10.1130/0016-7606(1989)101<0635:TDOG>2.3.CO;2, 1989.

673 Pan, Z.J., Zhang, Q., Chen, G., Jiao, S.T., Du, X.L., Miao, X.Q., Wang, J.R., and An, Y.: Relation
674 between Mesozoic magmatism and plate subduction in eastern China: Comparison among
675 Zhejiang-Fujian, Japan arc and Andes arc. Acta Petrol. Sin. (in Chinese with English abstract), 33,
676 1507–1523, 2017.

677 Peacock, S.M., Rushmer, T., and Thompson, A.B.: Partial melting of subducting oceanic crust. Earth
678 Planet. Sci. Lett., 121, 227-244. https://doi.org/10.1016/0012-821X(94)90042-6, 1994.

679 Pearce, J.A.: Role of the sub-continental lithosphere in magma genesis at active continental margins.
680 In: Hawkesworth, C.J., Norry, M.J. (Eds.): Continental Basalts and Mantle Xenoliths. Shiva
681 Publishing Ltd., Nantwich, 230–249. ISBN: 978-0906812341, 1983.

682 Pearce, J.A., and Peate, D.W.: Tectonic implications of the composition of volcanic arc magmas. Annu.
683 Rev. Earth Planet. Sci., 23, 251–285. https://doi.org/10.1146/annurev.ea.23.050195.001343, 1995.

684 Peccerillo, A., and Taylor, S.R.: Geochemistry of Eocene calcalkaline volcanic rocks from the
685 Kastamonu area, northern Turkey. Contrib. Mineral. Petrol., 58, 130–143.
686 https://doi.org/10.1007/BF00384745, 1976.

687 Peng, P., Zhai, M.G., Zhang, H.F., Zhao, T.P., and Ni, Z.Y.: Geochemistry and geological significance
688 of the 1.8 Ga mafic dyke swarms in the North China Craton: an example from the juncture of
689 Shanxi, Hebei and Inner Mongolia. Acta Petrol. Sin. (in Chinese with English abstract), 20,
690 439-456, 2004.

691 Peng, P., Zhai, M.G., Guo, J.H., Kusky, T., and Zhao, T.P.: Nature of mantle source contributions and
692 crystal differentiation in the petrogenesis of the 1.78 Ga mafic dykes in the central North China
693 craton. Gondwana Res., 12, 29-46. https://doi.org/10.1016/j.gr.2006.10.022, 2007.

694 Peng, P., Zhai, M.G., Ernst, R.E., Guo, J.H., Liu, F., and Hu, B.: A 1.78 Ga large igneous province in
695 the North China craton: The Xiong'er Volcanic Province and the North China dyke swarm. Lithos,
696 101, 260-280. https://doi.org/10.1016/j.lithos.2007.07.006, 2008.

697 Petford, N., and Atherton, M.: Na-rich partial melts from newly underplated basaltic crust: the
698 Cordillera Blanca Batholith, Peru. J. Petrol., 37, 1491-1521.
699 https://doi.org/10.1093/petrology/37.6.1491, 1996.

Rapp, R.P., and Watson, E.B.: Dehydration melting of metabasalt at 8–32 kbar: Implications for continental growth and crust-mantle recycling. J. Petrol., 36, 891-931. https://doi.org/10.1093/petrology/36.4.891, 1995.

Reubi, O., and Blundy, J.: A dearth of intermediate melts at subduction zone volcanoes and the petrogenesis of arc andesites. Nature, 461, 1269-1273. https://doi.org/10.1038/nature08510, 2009.

Roberts, M.P., and Clemens, J.D.: Origin of high-potassium, calc-alkaline, I-type granitoids. Geology, 21, 825–828. https://doi.org/10.1130/0091-7613(1993)021<0825:OOHPTA>2.3.CO;2, 1993.

Schulz, B., Klemd, R., and Brätz, H.: Host rock compositional controls on zircon trace element signatures in metabasites from the Austroalpine basement. Geochim. Cosmochim. Acta, 70, 697–710. https://doi.org/10.1016/j.g*ca.*2005.10.001, 2006.

Shannon, R.D.: Revised effective ionic-radii and systematic studies of interatomic distances in halides and chalcogenides. Acta Crystallogr. A, 32, 751-767. https://doi.org/10.1107/S0567739476001551, 1976.

Shen, F.N.: The discovery of unconformity within the Taihua Group and definition of its stratigraphic sequence in the Lushan area, Henan. Reg. Geol. China (in Chinese with English abstract), 2, 135-140. doi: 10.12097/gbc.ZQYD402.005, 1994.

Siebel, W., Reitter, E., Wenzel, T., and Blaha U.: Sr isotope systematics of K-feldspars in plutonic rocks revealed by the Rb–Sr microdrilling technique. Chem. Geol., 222, 183–199. https://doi.org/10.1016/j.chemgeo.2005.06.012, 2005.

Stern, C., and Kilian, R.: Role of the subducted slab, mantle wedge and continental crust in the generation of adakites from the Andean Austral Volcanic Zone. Contrib. Mineral. Petrol., 123, 263-281. https://doi.org/10.1007/s004100050155, 1996.

Streck, M.J., Leeman, W.P., and Chesley, J.: High-magnesian andesite from Mount Shasta: A product of magma mixing and contamination, not a primitive mantle melt. Geology, 35, 351-354. https://doi.org/10.1130/G23286A.1, 2007.

Sun, Q.Y., Zhou, Y.Y., Wang, W., Li, C.D., and Zhao, T.P.: Formation and evolution of the Paleoproterozoic meta-mafic and associated supracrustal rocks from the Lushan Taihua Complex, southern North China Craton: Insights from zircon U-Pb geochronology and whole-rock geochemistry. Precambrian Res., 303,428-444. https://doi.org/10.1016/j.precamres.2017.05.018, 2017.

Sun, S.S., and McDonough, W.F.: Chemical and isotopic systematics of oceanic basalts: implications for mantle composition and processes. Geol. Soc. London, Spec. Publ., 42, 313-345. https://doi.org/10.1144/GSL.SP.1989.042.01.19, 1989.

Vermeesch, P.: IsoplotR: A free and open toolbox for geochronology. Geoscience Frontiers, 9, 1479-1493. https://doi.org/10.1016/j.gsf.2018.04.001, 2018.

Wan, Y.S., Wlide, S., Liu, D.Y., Yang, C.X., Song, B., and Yin, X.Y.: Further evidence for ~1.85 Ga metamorphism in the Central Zone of the North China Craton: SHRIMP U–Pb dating of zircon from metamorphic rocks in the Lushan area, Henan Province. Gondwana Res., 9, 189-197, https://doi.org/10.1016/j.gr.2005.06.010, 2006

Wang, C.M., Lu, Y.J., He, X.Y., Wang, Q.H., and Zhang, J.: The Paleoproterozoic diorite dykes in the southern margin of the North China Craton: Insight into rift-related magmatism. Precambrian Res., 277, 26-46. https://doi.org/10.1016/j.precamres.2016.02.009, 2016.

Wang, J.L., Zhang, H.F., Zhang, J., Santosh, M., and Bao, Z. A.: Highly heterogeneous Pb isotope composition in the Archean continental lower crust: Insights from the high-grade metamorphic suite of the Taihua Group, Southern North China Craton. Precambrian Res., 350, 105927. https://doi.org/10.1016/j.precamres.2020.105927, 2020.

Wang, M.X., Wang Z.Y., Zhao J.X., Qi Z.Q., He J., and Chen F.K.: Petrogenesis and Geologic Implication of the Late Paleoproterozoic A-type Xiaohe Pluton along the Southern Margin of the North China Craton. Geol. J. China Univ. (in Chinese with English abstract), 29(6): 809-830, 2023a.

Wang, X., Huang X., and Yang F.: Revisiting the Lushan-Taihua Complex: New perspectives on the Late Mesoarchean-Early Neoarchean crustal evolution of the southern North China Craton: Precambrian Res., 325, 132–149. https://doi.org/10.1016/j.precamres.2019.02.020, 2019.

Wang, X.W., Zhu, M. Luo, X. Ren, and X. Cui.: Approximately 1.78 Ga mafic dykes in the Lüliang Complex, North China Craton: Zircon ages and Lu-Hf isotopes, geochemistry, and implications, Geochem. Geophys. Geosyst., 15, 3123–3144. doi:10.1002/2014GC005378, 2014.

Wang, X.L., Jiang, S.Y., and Dai, B.Z.: Melting of enriched Archean subcontinental lithospheric mantle: Evidence from the *ca.* 1760 Ma volcanic rocks of the Xiong'er Group, southern margin of the North China Craton. Precambrian Res., 182, 204–216. https://doi.org/10.1016/j.precamres.2010.08.007, 2010.

Wang, Y.J., Fan, W.M., Zhang, Y., Guo, F., Zhang, H., and Peng, T.: Geochemical, 40Ar/39Ar geochronological and Sr-Nd isotopic constraints on the origin of Paleoproterozoic mafic dikes from the southern Taihang Mountains and implications for the *ca.* 1800 Ma event of the North China Craton. Precambrian Res., 135, 55-77. https://doi.org/10.1016/j.precamres.2004.07.005, 2004.

Wang, Y., Zhao, G., Cawood, P. A., Fan, W., Peng, T., and Sun, L.: Geochemistry of Paleoproterozoic (~1770 Ma) mafic dikes from the Trans-North China Orogen and tectonic implications, J. Asian Earth Sci. 33(1–2), 61–77, https://doi.org/10.1016/j.jseaes.2007.10.018, 2008.

Wang, Z.Y., Zhao, J.X., Qi, Z.Q., Huo, D.Y., Siebel, W., He, J., Li, S.Q., and Chen, F.C.: Two stages of late Paleoproterozoic A-type granites at the southern North China Craton: Geochemical constraints and implications for supercontinent breakup, Precambrian Research, 411, 107500, https://doi.org/10.1016/j.precamres.2024.107500, 2024.

Wang, Z.Y., Cheng, H., Zhao, J.X., Ye R.S., Li W.Y., He J.F., and Chen F.K.: Sr-Nd-Pb isotopic composition of the Chinese national standard igneous rock powders measured by thermal ionization mass spectrometry. Geol. J. China Univ. (in Chinese with English abstract), 29, 679-692, 2023b.

Wolf, M.B., and Wyllie, P.J.: Garnet growth during amphibolite anatexis: Implications of a garnetiferous restite. J. Geol., 101, 357-373. https://doi.org/10.1086/648229, 1993.

Wolf, M., Romer, R.L., and Glodny, J.: Isotope disequilibrium during partial melting of metasedimentary rocks. Geochim. Cosmochim. Acta 257, 163-183. https://doi.org/10.1016/j.g*ca.*2019.05.008, 2019.

778 Xu, J.H., Jiang, Y.P., Hu, S.L., Zhang Z.W., Wu C.Q., Zheng C.F., Li X.Y., Jin Z.R., Zhang S.S., and
779 Zhou Y.T.: Petrogenesis and Tectonic Implications of the Paleoproterozoic A-Type Granites in the
780 Xiong'ershan Area along the Southern Margin of the North China Craton. J. Earth Sci., 35, 416–
781 429. https://doi.org/10.1007/s12583-021-1424-0, 2024.

782 Xu, Y.H., Zhao, T.P., Zhang, Y.X., and Chen, W.: Geochemical characteristics and geological
783 significance of the detrital rocks from the Dagushi Formation of the Paleoproterozoic Xiong'er
784 Group in the southern North China Craton, Geological Review, 54(3), 316–326,
785 https://doi.org/10.3321/j.issn:0371-5736.2008.03.004, 2008.

786 Xue, L.W., Yuan, Z.L., Zhang, M.S., and Qiang, L.Z.: The Sm-Nd isotope ages of Tai-hua Group in the
787 Lushan area and their implications. Geochimica (in Chinese with English abstract), 24, 92-97, 1995.

788 Yang, J.H., Cawood, P.A., Du, Y.S., Huang, H., Huang, H.W., and Tao, P.: Large Igneous Province and
789 magmatic arc sourced Permian–Triassic volcanogenic sediments in China. Sedimentary Geol.
790 261-262, 120-131. https://doi.org/10.1016/j.sedgeo.2012.03.018, 2012.

791 Yang, Z.M., Lu, Y.J., Hou, Z.Q., and Chang, Z.S.: High-Mg diorite from Qulong in southern Tibet:
792 implications for the genesis of adakite-like intrusions and associated porphyry Cu deposits in
793 collisional orogens. J. Petrol., 56, 227–254. https://doi.org/10.1093/petrology/egu076, 2015.

794 Zeng, L.S., Asimow, P.D., and Saleeby, J.B.: Coupling of anatectic reactions and dissolution of
795 accessory phases and the Sr and Nd isotope systematics of anatectic melts from a metasedimentary
796 source. Geochim. Cosmochim. Acta, 69, 3671-3682. https://doi.org/10.1016/j.g*ca*.2005.02.035,
797 2005.

798 Zhai, M.G.: Tectonic evolution and metallogenesis of North China Craton. Mineral Deposits (in
799 Chinese with English abstract), 29, 24-36, 2010.

800 Zhai M G.: Cratonization and the Ancient North China Continent: A summary and review. Sci China
801 Earth Sci (in Chinese with English abstract), 54: 1110–1120, doi: 10.1007/s11430-011-4250-x,
802 2011.

Zhao, G.C., Cawood, P.A., Wilde, S.A., Min, S., and Lu, L.Z.: Metamorphism of basement rocks in the Central Zone of the North China Craton: implications for Paleoproterozoic tectonic evolution. Precambrian Res., 103, 55-88. https://doi.org/10.1016/S0301-9268(00)00076-0, 2000a.

Zhao, G.C., He, Y.H., and Sun, M.: Xiong'er volcanic belt at the North China Craton: The Xiong'er volcanic belt at the southern margin of the North China Craton: Petrographic and geochemical evidence for its outboard position in the Paleo-Mesoproterozoic Columbia Supercontinent. Gondwana Res., 16, 170–181. https://doi.org/10.1016/j.gr.2009.02.004, 2009.

Zhao, G.C., Wilde, S.A., Cawood, P.A., and Lu, L.Z.: Petrology and P-T path of the Fuping mafic granulites: implications for tectonic evolution of the central zone of the North China Craton. J. Metamorphic Geol., 18, 375-391. https://doi.org/10.1046/j.1525-1314.2000.00264.x, 2000b.

Zhao, G.C., Wilde, S.A., Cawood, P.A., and Sun, M.: Archean blocks and their boundaries in the North China Craton: lithological, geochemical, structural and P–T path constraints and tectonic evolution. Precambrian Res. 107, 45-73. https://doi.org/10.1016/S0301-9268(00)00154-6, 2001.

Zhao, G.C., Wilde, S. A., Sun, M., Li, S., Li, X., and Zhang, J.: SHRIMP U–Pb zircon ages of granitoid rocks in the Lüliang Complex: Implications for the accretion and evolution of the Trans-North China Orogen, Precambrian Research, 160(3–4), 213–226, https://doi.org/10.1016/j.precamres.2007.07.004, 2008.

Zhao, G.C., Sun, M., Wilde, S.A., and Li Sanzhong.: Late Archean to Paleoproterozoic evolution of the North China Craton: key issues revisited. Precambrian Res., 136, 177-202 https://doi.org/10.1016/j.precamres.2004.10.002, 2005.

Zhao, G.C., and Zhai, M.G.: Lithotectonic elements of Precambrian basement in the North China Craton: Review and tectonic implications. Gondwana Res., 23, 1207-1240. https://doi.org/10.1016/j.gr.2012.08.016, 2013.

Zhao, J., Zhang, C., Guo, X., and Liu, X.: The late-Paleoproterozoic I- and A-type granites in Lüliang Complex, North China Craton: New evidence on post-collisional extension of Trans-North China Orogen, Precambrian Research, 318, 70–88, https://doi.org/10.1016/j.precamres.2018.09.007, 2018.

Zhao, T.P.: The characteristic and genesis of Proterozoic potassic volcanic rock in southern margin of the North plate. Doctoral dissertation, Institute of Geology and Geophysics, Chinese Academy of Sciences, Beijing, 102p, 2000.

Zhao, T.P., Xu, Y.H., and Zhai, M.G.: Petrogenesis and tectonic setting of the Paleoproterozoic Xiong'er Group in the southern part of the North China Craton: A review. Geol. J. China Univ. (in Chinese with English abstract), 13, 191–206, 2007.

Zhao, T.P., Zhou, M.F., Zhai, M.G., and Xia, B.: Paleoproterozoic rift-related volcanism of the Xiong'er Group, North China Craton: Implications for the breakup of Columbia. Int. Geol. Rev., 44, 336-351. https://doi.org/10.2747/0020-6814.44.4.336, 2002

Zhao, T.P., Zhai, M.G., Xia, B., Li, H.M., and Zhang, Y.X.: Zircon U-Pb SHRIMP dating for the volcanic rocks of the Xiong'er Group: Constraints on the initial formation age of the cover of the North China Craton. Chin. Sci. Bull. (in Chinese with English abstract), 49, 2495–2502, 2004.

Zhang, G.W., Bai, Y.B., Sun, Y., Guo, A.L., Zhou, D.W., and Li, T.H.: Composition and evolution of the Archaean crust in central Henan, China. Precambrian Res., 27, 7-35. https://doi.org/10.1016/0301-9268(85)90004-X, 1985.

Zou, X.Y., Qin, K.Z., Han, X.L., Li, G.M., Evans, N.J., Li, Z.Z., and Yang, W.: Insight into zircon REE oxy-barometers: A lattice strain model perspective. Earth Planet. Sci. Lett., 506, 87-96. https://doi.org/10.1016/j.epsl.2018.10.031, 2019.

Figure

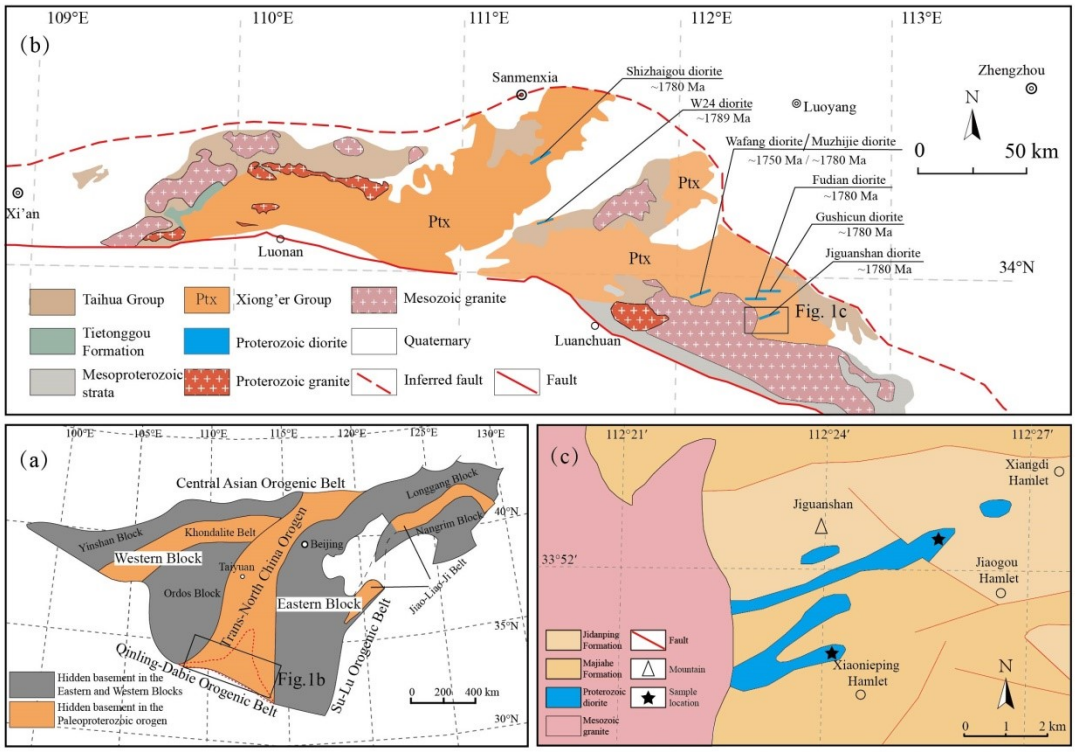

Figure 1 (a) Tectonic sketch of the North China Craton (after Zhao et al., 2001); (b) Geological map of the southern margin of the North China Craton (after Diwu et al., 2014; diorites from Cui et al., 2011; Ma et al 2023a, b; Wang et al., 2016; Zhao et al., 2004); (c) Geological map of the Jiguanshan diorite (after BGMRH, 1994)

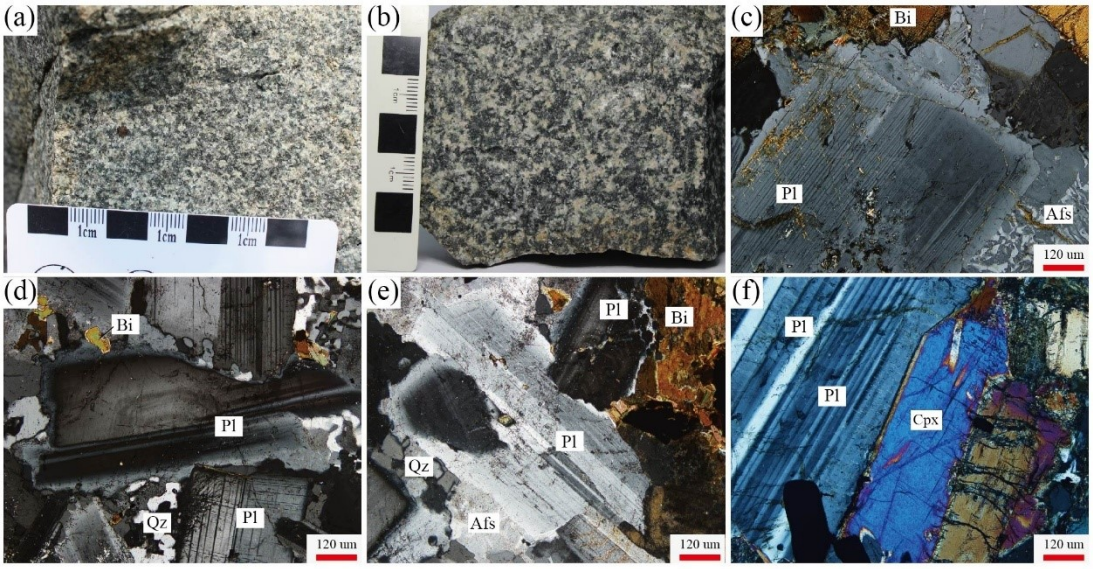

857

858 **Figure 2** (a-b) Field photographs and representative hand specimens of the Jiguanshan diorite; (c-f)

859 Microphotographs under plane-polarized light of the Jiguanshan diorite. Mineral

860 abbreviations: Afs, alkali feldspar; Bi, biotite; Cpx, Clinopyroxene; Pl, plagioclase; Qz,

861 quartz

862

863

864

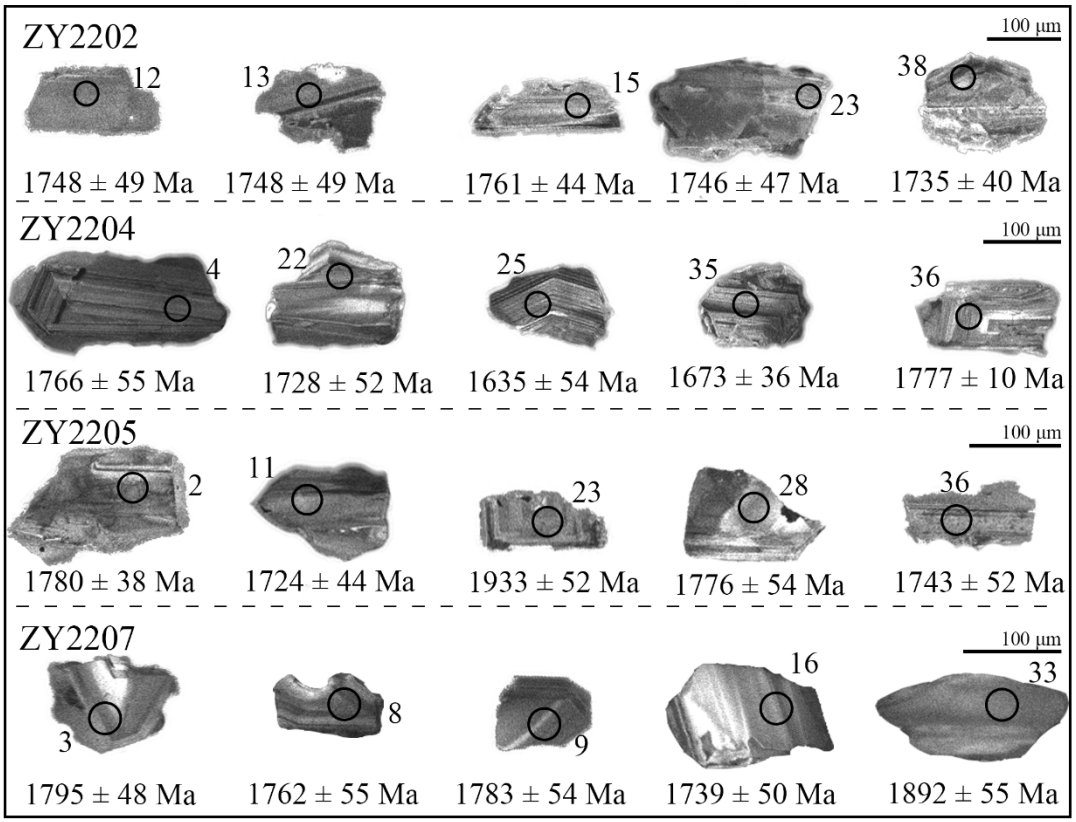

865

866 **Figure 3** Cathodoluminescence (CL) images of representative zircon grains from the Jiguanshan

867 diorite

868

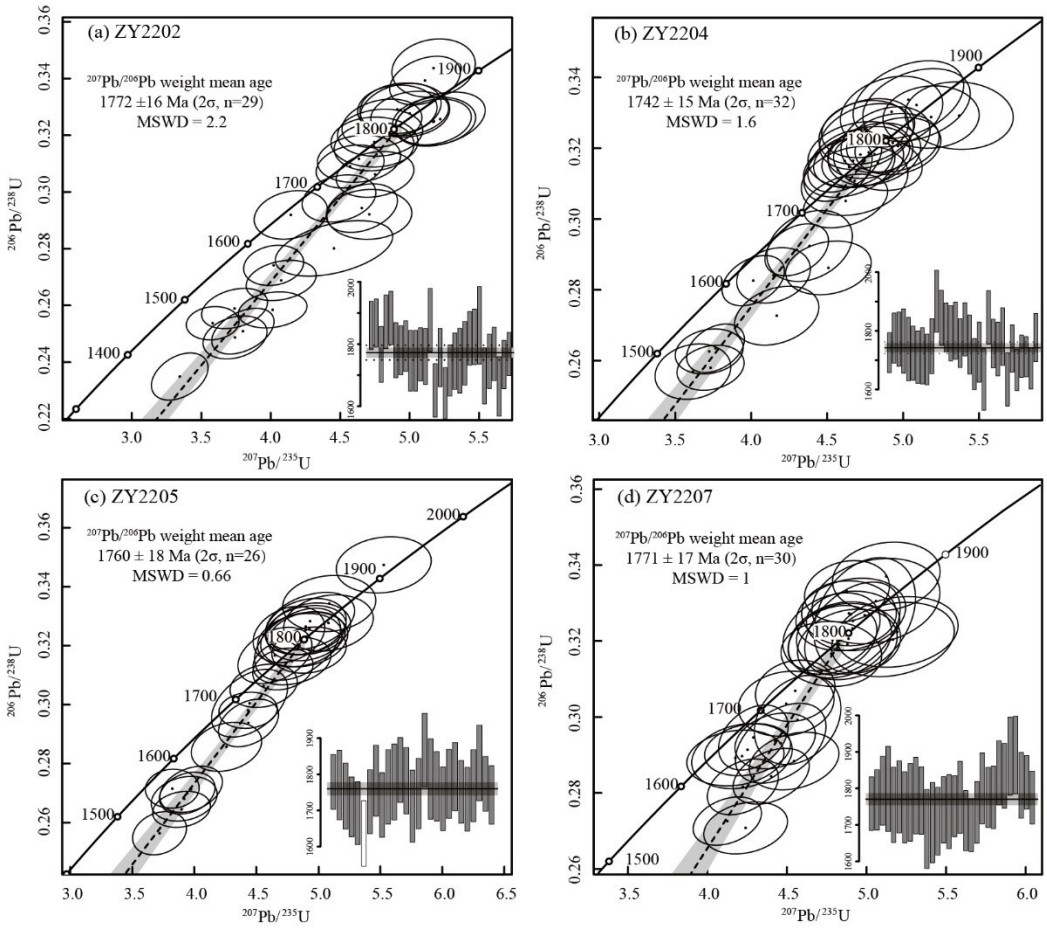

869

870 **Figure 4** (a-d) Zircon U–Pb Concordia diagrams for the Jiguanshan diorite

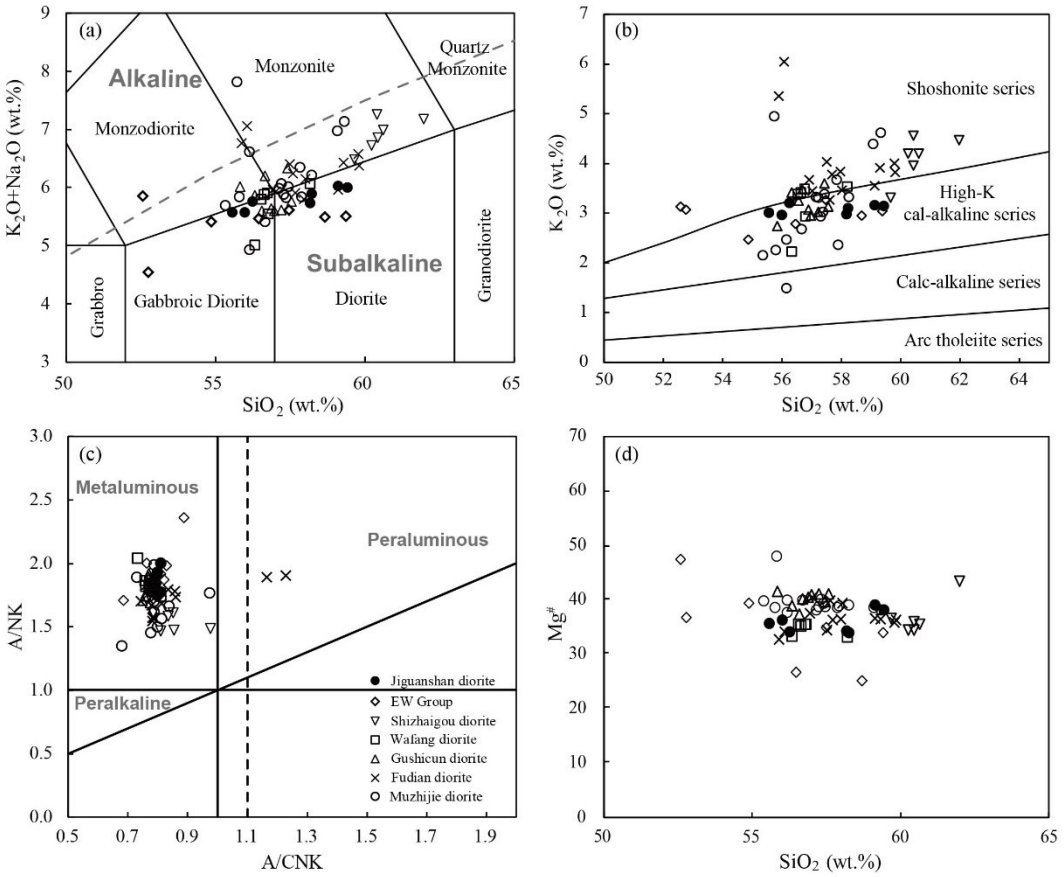

871

872 **Figure 5** Plots of major elements for the diorites: (a) TAS diagram (after Le Bas et al., 1986); (b)
873 K_2O content (wt. %) versus SiO_2 content (wt. %) (after Peccerillo and Taylor, 1976); (c)
874 A/NK versus A/CNK values (after Maniar and Piccoli, 1989) (d) $Mg^{\#}$ value versus SiO_2
875 content (wt. %)

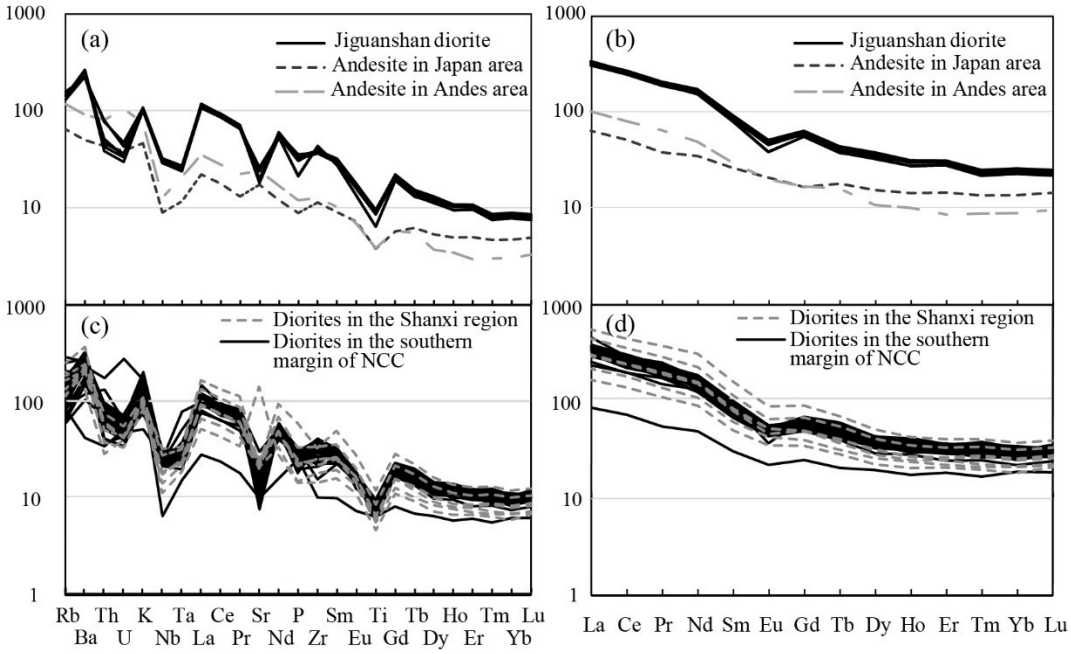

876

877 **Figure 6** Primitive-mantle normalized trace element spider diagrams and chondrite-normalized
878 REE patterns for the diorites. Normalization values from Sun and McDonough (1989);
879 Diorites in Shanxi region from Peng et al. (2007), diorites in the southern margin of the NCC
880 from Cui et al. (2011), Ma et al. (2023a, b), Wang et al. (2016), and Zhao et al. (2004).
881 Average trace element compositions of intermediate rocks in the Japan and Andes arc are
882 from Pan et al. (2017)

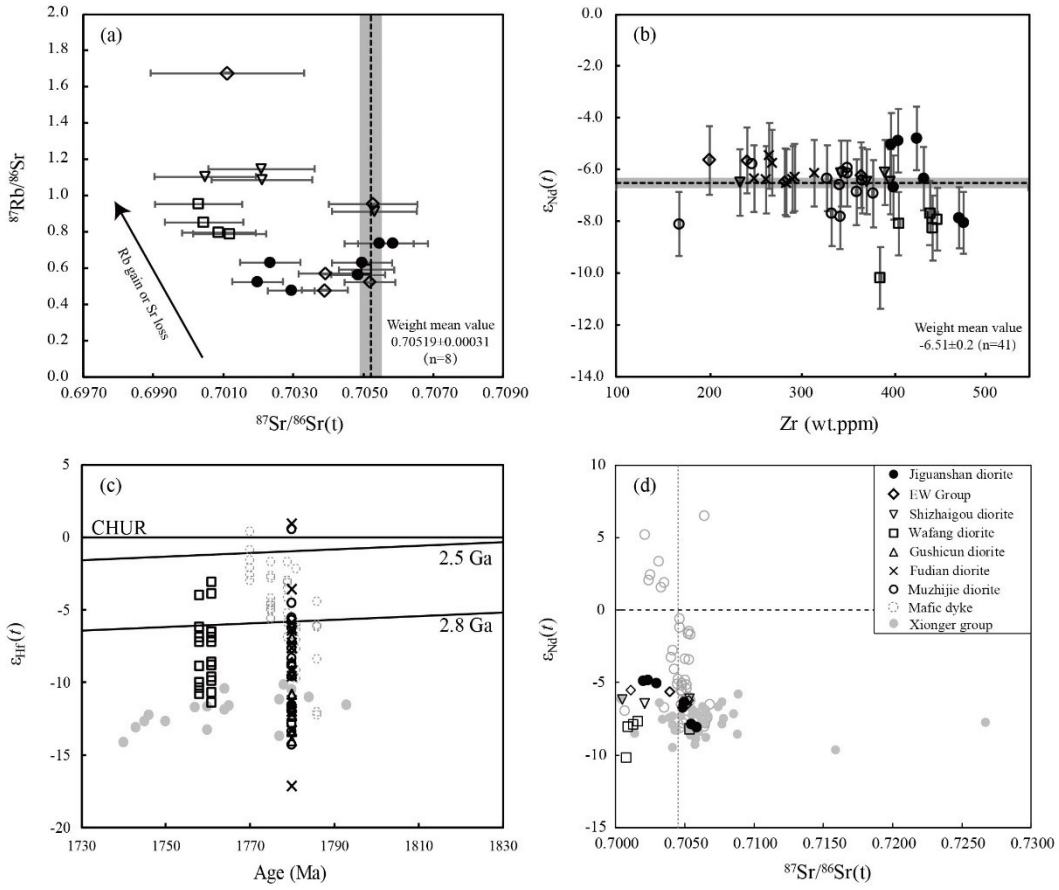

883

884 **Figure 7** (a) $^{87}Rb/^{86}Sr$ versus $^{87}Sr/^{86}Sr(t)$ ratio; (b) $\varepsilon_{Nd}(t)$ value versus Zr content (ppm); (c) $\varepsilon_{Hf}(t)$
885 value versus age (Ma); (d) $\varepsilon_{Nd}(t)$ value versus $^{87}Sr/^{86}Sr(t)$ ratio. Data source for Xiong'er
886 Group (Hf isotope composition from Wang et al., 2010; initial Sr isotope composition and
887 initial ε_{Nd} value from He et al., 2008, 2010; Peng et al., 2008; Wang et al., 2010; Zhao et al.,
888 2002); mafic dyke swarms (initial Sr isotope composition and initial ε_{Nd} value from Hu et al.,
889 2010; Peng et al., 2007; Wang et al., 2004)

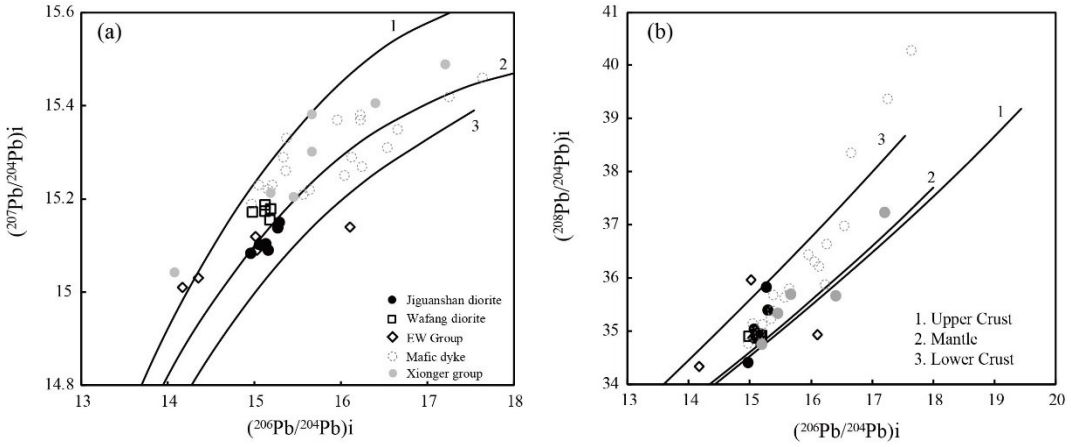

890

891 **Figure 8** (a) ($^{207}Pb/^{204}Pb$)i versus ($^{206}Pb/^{204}Pb$)i; (b) ($^{208}Pb/^{204}Pb$)i versus ($^{206}Pb/^{204}Pb$)i. Data for
892 Xiong'er Group from Zhao (2000), for mafic dyke swarms from Hu et al. (2010), Peng et al.,
893 (2007) and for diorites from Peng et al. (2007), Wang et al. (2016)

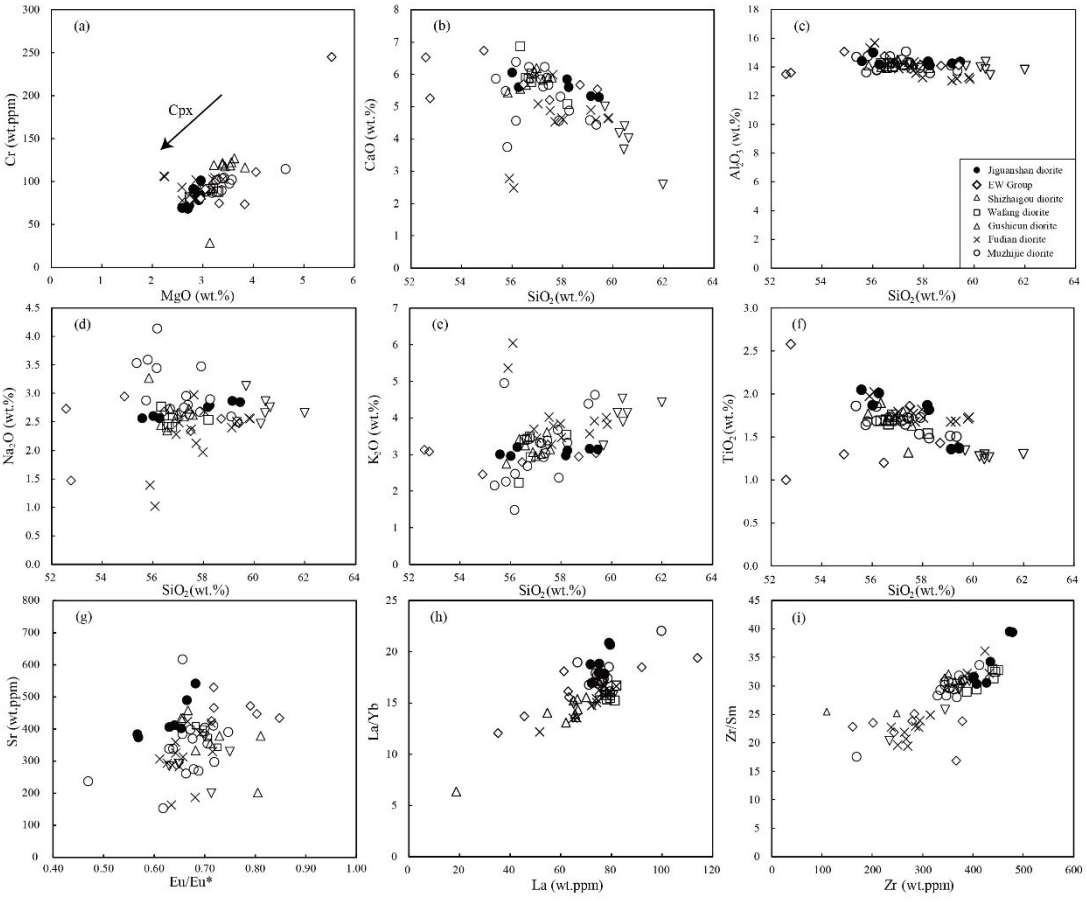

894

895 **Figure 9** (a) Cr (ppm) content versus MgO content (wt. %); (b) CaO (wt. %) content versus SiO_2
896 content (wt. %); (c) Al_2O_3 (wt. %) content versus SiO_2 content (wt. %); (d) Na_2O (wt. %)
897 content versus SiO_2 content (wt. %); (e) K_2O (wt. %) content versus SiO_2 content (wt. %); (f)

TiO_2 (wt. %) content versus SiO_2 content (wt. %); (g) Eu/Eu*value versus Sr content (ppm); (h) La/Yb value versus La content (ppm); (i) Zr/Sm value versus Zr content (ppm)

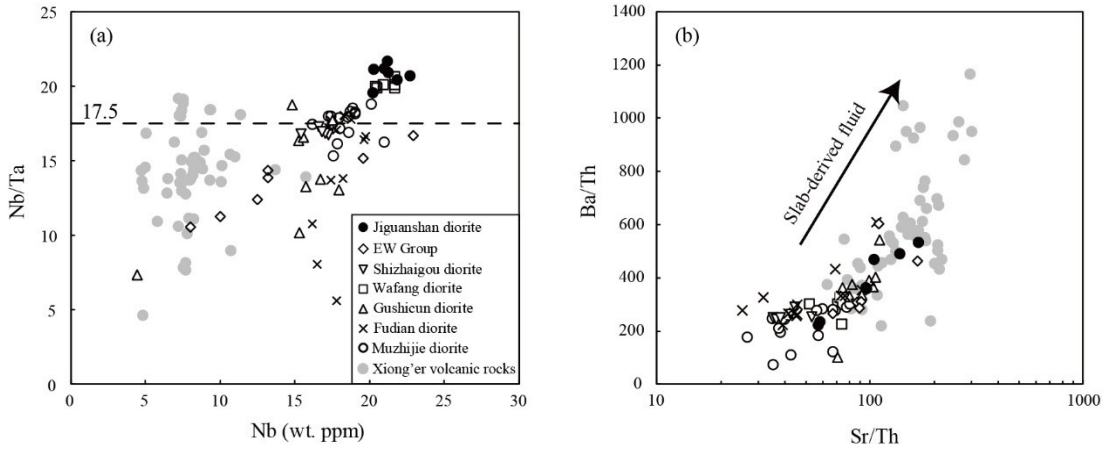

Figure 10 (a) Nb/Ta value versus Nb content (ppm); (b) Ba/Th value versus Sr/Th value; Data for Xiong'er Group from He et al. (2008, 2010), Wang et al. (2010), Zhao et al. (2002)

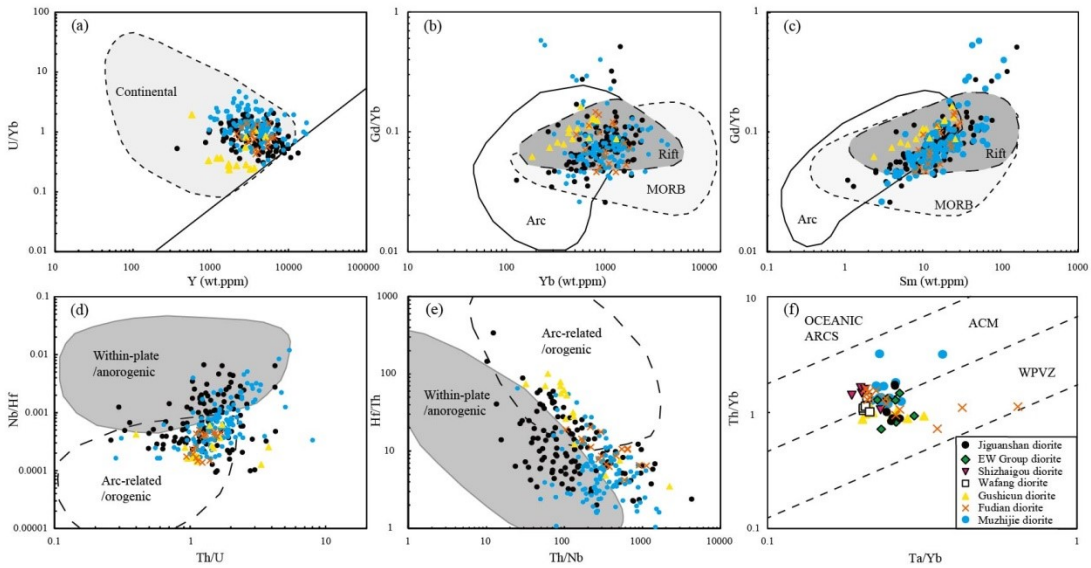

Figure 11 (a) Zircon trace element U/Yb ratio versus Y content (ppm) (after Grimes et al., 2007); (b) Zircon Gd/Yb ratio versus Yb content (ppm) (after Carley et al., 2014); (c) Zircon Gd/Yb ratio versus Sm content (ppm) (after Carley et al., 2014); (d) Zircon Nb/Hf ratio versus Th/U ratio (after Hawkesworth and Kemp, 2006); (e) Zircon Hf/Th ratio versus Th/Nb ratio (after Yang et al., 2012); (f) Whole-rock trace element Th/Yb ratio versus Ta/Yb ratio (after Pearce, 1983; Gorton and Schandl, 2000)

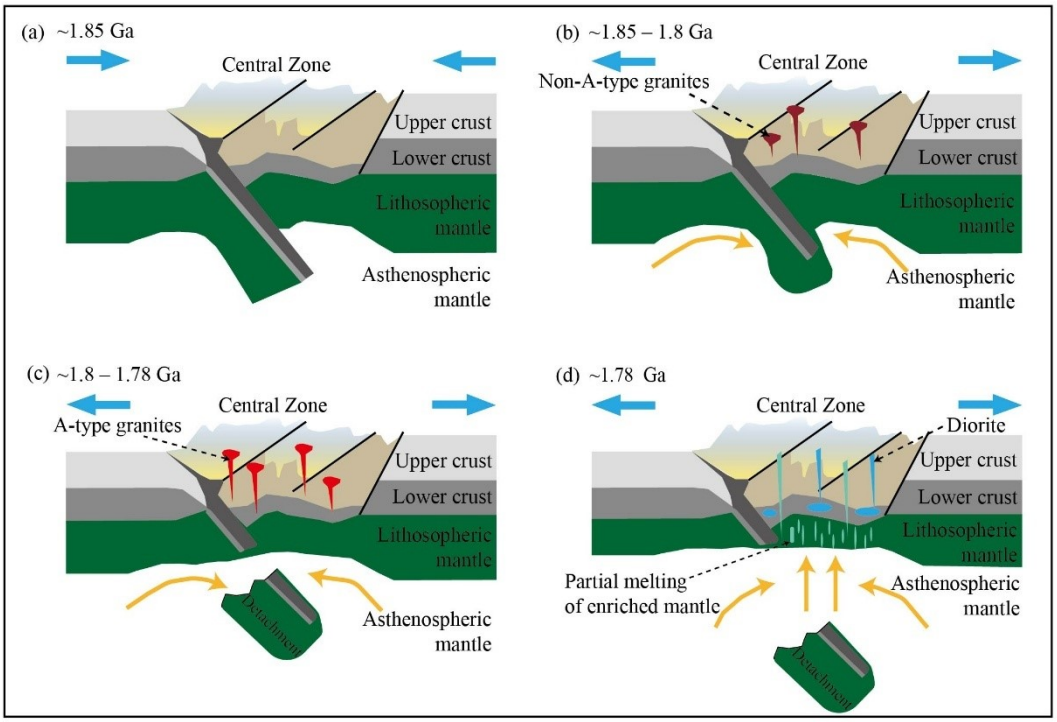

910

911 **Figure 12** Tectonic evolution in the North China Craton during the Paleoproterozoic (after Wang
912 et al., 2004; Deng et al., 2016): (a) ~1.85 Ga: Western and Eastern Blocks collision; (b)
913 ~1.85–1.8 Ga: Post-collisional crustal thickening and granite emplacement; (c) ~1.8–1.78 Ga:
914 Post-collisional delamination and formation of A-type granite; (d) ~1.78 Ga: Transition from
915 post-collisional to rift setting

916

917

Table

Table 1 Major (wt. %) and trace element contents (ppm) of the Jiguanshan diorite

Sample No.	ZY2201	ZY2202	ZY2203	ZY2204	ZY2205	ZY2206	ZY2207
(wt.%)							
SiO_2	58.18	59.44	59.13	58.24	56.26	56.01	55.57
TiO_2	1.87	1.37	1.36	1.82	2.01	1.87	2.05
Al_2O_3	14.38	14.37	14.24	14.11	14.18	15.00	14.41
$^{T}Fe_2O_3$	10.38	9.04	9.17	10.00	10.35	10.18	10.50
MnO	0.15	0.14	0.14	0.14	0.17	0.14	0.15
MgO	2.73	2.81	2.96	2.59	2.70	2.92	2.94
CaO	5.85	5.29	5.33	5.60	5.61	6.06	5.81
Na_2O	2.76	2.85	2.87	2.79	2.56	2.60	2.56
K_2O	2.98	3.15	3.16	3.11	3.21	2.97	3.01
P_2O_5	0.71	0.46	0.45	0.65	0.73	0.68	0.76
LOI	0.48	1.31	0.67	0.36	1.53	1.60	1.67
Total	100.47	100.23	99.48	99.41	99.31	100.03	99.43
(ppm)							
Li	11.2	19.8	19.9	14.8	18.6	20.7	18.2
Be	2.66	2.80	2.76	2.94	3.06	2.70	2.97
Sc	22.7	20.1	20.4	23.3	24.3	24.0	23.8
V	163	141	147	168	179	165	164
Cr	72.1	91.3	101.3	69.5	68.6	78.6	83.5
Ni	21.3	22.3	24.0	20.7	19.2	20.2	21.6
Cu	20.8	19.8	19.9	20.9	27.0	22.2	23.3
Zn	131	128	122	133	148	139	141
Ga	21.9	21.9	21.8	22.9	23.3	23.8	22.7
Rb	80.3	95.2	97.8	88.4	88.0	89.5	88.9
Sr	412	374	384	406	403	542	490
Y	47.5	44.4	43.8	48.4	49.3	44.8	46.7
Zr	402	478	474	435	428	400	407
Nb	20.2	21.2	21.0	21.2	22.7	20.3	21.8
Cs	0.60	0.77	0.74	0.95	2.98	3.63	4.44
Ba	1543	1515	1504	1544	1814	1714	1737
La	72.2	79.0	79.5	75.0	77.3	71.7	75.2
Ce	149	161	161	154	163	150	159
Pr	17.6	18.3	18.1	18.2	19.4	18.0	18.9
Nd	72.3	71.2	70.9	73.2	80.0	72.9	77.1
Sm	12.7	12.1	12.0	12.7	14.0	12.8	13.4
Eu	2.63	2.21	2.18	2.59	2.93	2.78	2.87
Gd	12.1	11.2	11.2	12.1	13.0	11.7	12.5

Tb	1.53	1.39	1.40	1.51	1.63	1.47	1.56
Dy	8.99	8.32	8.11	8.92	9.50	8.53	9.00
Ho	1.67	1.54	1.53	1.67	1.75	1.53	1.65
Er	4.97	4.56	4.54	4.95	5.09	4.55	4.87
Tm	0.62	0.55	0.55	0.60	0.63	0.55	0.58
Yb	4.26	3.79	3.84	4.18	4.33	3.82	3.99
Lu	0.61	0.55	0.56	0.60	0.63	0.55	0.58
Hf	7.97	9.09	9.15	8.20	8.46	7.59	7.98
Ta	1.03	0.98	0.99	1.01	1.10	0.96	1.07
Pb	16.4	21.2	18.0	16.3	18.9	15.2	14.2
Th	4.28	6.43	6.71	4.27	3.87	3.22	3.55
U	0.70	0.98	0.88	0.71	0.75	0.61	0.68
K_2O/Na_2O	1.08	1.11	1.10	1.11	1.25	1.14	1.18
K_2O+Na_2O (Wt.%)	5.74	6.00	6.03	5.90	5.77	5.57	5.57
Mg#	34.5	38.3	39.2	34.1	34.3	36.5	35.9
A/CNK	0.78	0.81	0.80	0.78	0.79	0.81	0.80
A/NK	1.85	1.77	1.75	1.77	1.84	2.00	1.93
ΣREE	361.5	375.8	375.1	370.4	393.2	361.2	381.3
Eu/Eu*	0.64	0.57	0.57	0.63	0.65	0.68	0.66
$(La/Yb)_N$	12.2	15.0	14.8	12.9	12.8	13.5	13.5

$Mg^{\#}=(MgO+FeO_{total})/MgO\times100$

$Eu/Eu^{*}=2Eu_N/(Sm_N+Gd_N)$; $(La/Yb)_N$=chondrite-normalized La/Yb ratio

920

921

922 **Table 2** Whole-rock Sr isotopic compositions of the late Paleoproterozoic diorites in the NCC

Sample	Age (Ma)	Rb (ppm)	Sr (ppm)	Rb/Sr	$^{87}Rb/^{86}Sr$	$^{87}Sr/^{86}Sr$	±2SE	$^{87}Sr/^{86}Sr$ (t)	Error (abs.)	Data source
Jiguanshan diorite										
ZY2201	1780	80.3	412	0.20	0.5648	0.71931	0.000010	0.70485	0.00077	
ZY2202	1780	95.2	374	0.25	0.7371	0.72471	0.000012	0.70584	0.00099	
ZY2203	1780	97.8	384	0.25	0.7377	0.72434	0.000011	0.70546	0.00099	
ZY2204	1780	88.4	406	0.22	0.6307	0.72111	0.000011	0.70496	0.00085	This study
ZY2205	1780	88.0	403	0.22	0.6334	0.71856	0.000011	0.70235	0.00086	
ZY2206	1780	89.5	542	0.17	0.4780	0.71518	0.000011	0.70294	0.00066	
ZY2207	1780	88.9	490	0.18	0.5252	0.71542	0.000013	0.70198	0.00072	
Wafang diorote										
WF1307-3	1780	107.0	389	0.28	0.7969	0.72131	0.000013	0.70091	0.00106	
WF1307-4	1780	109.0	400	0.27	0.7895	0.72144	0.000014	0.70123	0.00105	
WF1307-5	1780	84.0	411	0.20	0.5921	0.72024	0.000016	0.70508	0.00080	Wang et al. (2016)
WF1307-8	1780	113.0	343	0.33	0.9548	0.72479	0.000016	0.70035	0.00127	
WF1307-9	1780	110.0	373	0.29	0.8545	0.72236	0.000014	0.70048	0.00114	
Shizhaigou diorite										
Ln-1	1780	103.7	272	0.38	1.1040	0.72874	0.000012	0.70048	0.00146	
Ln-2	1780	101.5	322	0.31	0.9125	0.72868	0.000015	0.70532	0.00121	Cui et al. (2011)
Ln-3	1780	136.4	200	0.68	1.9758	0.72509	0.00001	0.67452	0.00259	

Ln-4	1780	116.6	295	0.40	1.1479	0.73149	0.000015	0.70210	0.00152	
Ln-5	1780	112.5	300	0.38	1.0885	0.72997	0.000014	0.70211	0.00144	
E-W Group dyke										
02SX001	1780	154.8	470	0.33	0.9542	0.72970	0.000014	0.70528	0.00127	
02SX007	1780	81.2	450	0.18	0.5231	0.71858	0.000014	0.70519	0.00072	
03LF01	1780	74.4	449	0.17	0.4801	0.71619	0.000013	0.70390	0.00066	Peng et al. (2007)
03FS04	1780	131.8	229	0.58	1.6748	0.74399	0.000012	0.70112	0.00220	
03FS07	1780	106.0	539	0.20	0.5699	0.71852	0.000013	0.70393	0.00078	
Weight mean value								0.70519	0.00031	(n=8, calculated by IsoplotR)

$(^{87}Sr/^{86}Sr)_s = (^{87}Sr/^{86}Sr)_0 + (^{87}Rb/^{86}Sr)_s \times (e^{\lambda t} - 1)$

$\lambda_{87Rb} = 1.42\times10^{-11}/a^{-1}$

Error of initial ratio is calculated from the measurement error of the isotope ratio, the estimated concentration error and the age error. The decay constant is considered to be a fixed value.

$\sigma_{Sr(t)}$ is mean-square deviation of $(^{87}Sr/^{86}Sr)_t$

σ_{Rb} is mean-square deviation of $(^{87}Rb/^{86}Sr)_s$

σ_t is mean-square deviation of age

$$\sigma_{Sr(t)} = \sqrt{\sigma_{Sr}^2 + \sigma_{Rb}^2(e^{\lambda t} - 1)^2 + \sigma_t^2(\lambda e^{\lambda t}(\frac{87_{Rb}}{86_{Sr}}))^2}$$

923

924

925 **Table 3** Whole-rock Nd isotopic compositions of the late Paleoproterozoic diorites in the NCC

Sample	Age (Ma)	Nd (ppm)	Sm (ppm)	$^{147}Sm/^{144}Nd$	$^{143}Nd/^{144}Nd$	Error (2s)	$^{143}Nd/^{144}Nd$ (t)	Error (abs.)	$\varepsilon_{Nd}(t)$	Error (εNd)	T_{DM2} (Ga)	Data source
Jiguanshan diorite												
ZY2201	1780	72.3	12.7	0.1063	0.511238	0.000007	0.509994	0.000063	-6.69	1.24	2.83	
ZY2202	1780	71.2	12.1	0.1029	0.511129	0.000008	0.509924	0.000061	-8.04	1.20	2.94	
ZY2203	1780	70.9	12.0	0.1022	0.511131	0.000005	0.509934	0.000060	-7.85	1.19	2.93	
ZY2204	1780	73.2	12.7	0.1049	0.511240	0.000007	0.510011	0.000062	-6.35	1.22	2.80	This study
ZY2205	1780	80.0	14.0	0.1058	0.511329	0.000007	0.510090	0.000063	-4.80	1.23	2.68	
ZY2206	1780	72.9	12.8	0.1058	0.511317	0.000005	0.510078	0.000063	-5.03	1.23	2.70	
ZY2207	1780	77.1	13.4	0.1054	0.511320	0.000006	0.510086	0.000062	-4.88	1.22	2.68	
E-W Group dyke												
02SX001	1780	113	20.3	0.1084	0.511287	0.000009	0.510018	0.000065	-6.21	1.27	2.79	
02SX007	1780	62.6	11.3	0.1093	0.511285	0.000010	0.510005	0.000065	-6.47	1.28	2.81	
03LF01	1780	45.1	8.36	0.1120	0.511358	0.000017	0.510047	0.000068	-5.64	1.34	2.75	Peng et al. (2007)
03FS04	1780	102	17.5	0.1039	0.511270	0.000010	0.510053	0.000062	-5.53	1.22	2.74	
03FS07	1780	62.7	11.1	0.1068	0.511297	0.000013	0.510047	0.000064	-5.65	1.26	2.75	
Shizhaigou diorite												
Ln-1	1780	69.0	12.3	0.1075	0.511280	0.000012	0.510021	0.000065	-6.15	1.26	2.79	Cui et al. (2011)
Ln-2	1780	66.4	11.7	0.1065	0.511270	0.000011	0.510023	0.000064	-6.10	1.25	2.78	

Ln-3	1780	61.9	11.2	0.1090	0.511280	0.000011	0.510003	0.000065	-6.50	1.28	2.82	
Ln-4	1780	71.1	12.6	0.1072	0.511260	0.000011	0.510005	0.000064	-6.46	1.26	2.81	
Ln-5	1780	69.4	12.3	0.1072	0.511260	0.000012	0.510005	0.000064	-6.46	1.26	2.81	
Wafang diorote												
WF1307-3	1780	78.4	13.7	0.1056	0.511169	0.000008	0.509953	0.000062	-7.90	1.23	2.93	
WF1307-4	1780	78.5	14.1	0.1086	0.511215	0.000008	0.509965	0.000063	-7.67	1.26	2.91	
WF1307-5	1780	75.9	13.7	0.1091	0.511192	0.000008	0.509936	0.000064	-8.24	1.27	2.96	Wang et al. (2016)
WF1307-8	1780	77.6	13.4	0.1044	0.511039	0.000007	0.509837	0.000061	-10.2	1.21	3.11	
WF1307-9	1780	77.5	13.9	0.1084	0.511193	0.000005	0.509945	0.000063	-8.07	1.26	2.94	
Gushicun diorite												
20XRδ-1	1780	58.0	10.9	0.1134	0.511327	0.000004	0.509999	0.000067	-6.58	1.31	2.82	
20XRδ-3	1780	63.3	11.7	0.1118	0.511334	0.000006	0.510025	0.000066	-6.08	1.30	2.78	Ma et al. (2023a)
20XRδ-4	1780	59.1	10.9	0.1118	0.511341	0.000006	0.510032	0.000066	-5.94	1.30	2.77	
20XRδ-5	1780	53.1	9.9	0.1122	0.511354	0.000006	0.510041	0.000066	-5.77	1.30	2.76	
The Muzhijie diorites												
20δPt2-1	1780	63.5	11.5	0.1090	0.511297	0.000004	0.510021	0.000064	-6.15	1.26	2.79	
20δPt2-3	1780	64.2	11.7	0.1100	0.511300	0.000004	0.510012	0.000065	-6.33	1.27	2.80	
20δPt2-5	1780	66.4	12.3	0.1122	0.511295	0.000007	0.509982	0.000067	-6.92	1.30	2.85	
20δPt2-7	1780	72.1	13.1	0.1101	0.511297	0.000008	0.510007	0.000065	-6.42	1.28	2.81	Ma et al. (2023b)
20δPt2-9	1780	54.2	9.6	0.1076	0.511181	0.000006	0.509922	0.000064	-8.09	1.25	2.95	
20δPt2-11	1780	64.5	11.4	0.1073	0.511199	0.000006	0.509943	0.000064	-7.69	1.25	2.91	
20δPt2-13	1780	62.9	11.2	0.1076	0.511196	0.000008	0.509937	0.000064	-7.80	1.25	2.92	
20δPt2-16	1780	67.9	12.3	0.1098	0.511270	0.000007	0.509984	0.000065	-6.87	1.28	2.85	

Fudian diorite												
20XRSC-1	1780	65.8	12.1	0.1110	0.511309	0.000006	0.510009	0.000066	-6.39	1.29	2.81	
20XRSC-2	1780	67.1	12.3	0.1111	0.511315	0.000006	0.510014	0.000066	-6.30	1.29	2.80	
20XRSC-3	1780	69.5	12.8	0.1113	0.511314	0.000004	0.510011	0.000066	-6.35	1.29	2.80	
20XRSC-4	1780	67.5	12.5	0.1117	0.511311	0.000007	0.510002	0.000066	-6.52	1.30	2.82	Ma et al. (2023b)
20XRSC-5	1780	70.1	12.9	0.1111	0.511311	0.000006	0.510010	0.000066	-6.37	1.29	2.81	
20XRSC-6	1780	68.9	12.7	0.1112	0.511324	0.000005	0.510022	0.000066	-6.14	1.29	2.79	
20XRSC-8	1780	71.7	12.9	0.1089	0.511331	0.000006	0.510056	0.000065	-5.46	1.26	2.75	
20XRSC-9	1780	76.6	13.9	0.1096	0.511325	0.000005	0.510042	0.000065	-5.74	1.27	2.75	
Weight mean value									-6.51	0.20		(n =41, calculated by IsoplotR)

$(^{143}Nd/^{144}Nd)_s = (^{143}Nd/^{144}Nd)_0 + (^{147}Sm/^{144}Nd)_s \times (e^{\lambda t} - 1)$

$\varepsilon_{Nd}(t) = [(^{143}Nd/^{144}Nd)_t / (^{143}Nd/^{144}Nd)_{CHUR(t)} - 1] \times 10000$

$T_{DM2} = 1/\lambda \times Ln\{1 + [(^{143}Nd/^{144}Nd)_{DM} - (^{143}Nd/^{144}Nd)_S + ((^{147}Sm/^{144}Nd)_S - (^{147}Sm/^{144}Nd)_{CC}) \times (e^{\lambda t} - 1)] / ((^{147}Sm/^{144}Nd)_{DM} - (^{147}Sm/^{144}Nd)_{CC})\}$

$\lambda_{147Sm} = 0.654 \times 10^{-11}/a^{-1}$

$^{143}Nd/^{144}Nd)_{DM} = 0.51315$

$^{147}Sm/^{144}Nd)_{DM} = 0.2137$

$^{147}Sm/^{144}Nd)_{CC} = 0.12$

Error of initial ratio is calculated from the measurement error of the isotope ratio, the estimated concentration error and the age error. The decay constant is considered to be a fixed value.

$\sigma_{Nd(t)}$ is mean-square deviation of

$$\sigma_{Nd(t)} = \sqrt{\sigma_{Nd}^2 + \sigma_{Sm}^2 (e^{\lambda t} - 1)^2 + \sigma_t^2 (\lambda e^{\lambda t} (\frac{147_{Sm}}{144_{Nd}}))^2}$$

$(^{143}Nd/^{144}Nd)_t$

σ_{Sm} is mean-square deviation of $(^{143}Sm/^{144}Nd)_s$

σ_t is mean-square deviation of age

926

927

928 **Table 4** Whole-rock Pb isotopic compositions of the Jiguanshan diorite

Spon.no	U (ppm)	Th (ppm)	Pb (ppm)	$^{206}Pb/^{204}Pb$	±2SE	$^{207}Pb/^{204}Pb$	±2SE	$^{208}Pb/^{204}Pb$	±2SE	$^{206}Pb/^{204}Pb$ initial	$^{207}Pb/^{204}Pb$ initial	$^{208}Pb/^{204}Pb$ initial	$^{238}U/^{204}Pb$ μ	$^{232}Th/^{204}Pb$ ω	$^{232}Th/^{238}U$
ZY2201	0.70	4.28	16.38	15.867	0.0005	15.189	0.0005	36.502	0.0014	15.063	15.103	35.027	2.6	16.0	6.3
ZY2202	0.98	6.43	21.20	16.167	0.0008	15.243	0.0009	37.126	0.0022	15.295	15.150	35.392	2.8	18.8	6.8
ZY2203	0.88	6.71	18.03	15.882	0.0006	15.182	0.0006	36.494	0.0013	14.965	15.084	34.398	2.9	22.8	7.8
ZY2204	0.71	4.27	16.29	16.097	0.0010	15.225	0.0009	37.324	0.0023	15.271	15.137	35.825	2.6	16.3	6.2
ZY2205	0.75	3.87	18.90	15.832	0.0007	15.179	0.0006	36.046	0.0016	15.095	15.100	34.901	2.3	12.4	5.3
ZY2206	0.61	3.22	15.22	15.914	0.0010	15.170	0.0010	36.124	0.0024	15.164	15.090	34.939	2.4	12.9	5.4
ZY2207	0.68	3.55	14.22	16.036	0.0008	15.199	0.0007	36.338	0.0016	15.136	15.103	34.931	2.9	15.3	5.4

Initial Pb isotopic ratios are calculated back to 1780 Ma.

929